Event-by-event shape and flow fluctuations of relativistic heavy-ion collision fireballs

Zhi Qiu and Ulrich Heinz
Department of Physics, The Ohio State University, Columbus, OH 43210-1117, USA
(Dated: January 21, 2022)

Heavy-ion collisions create deformed quark-gluon plasma (QGP) fireballs which explode anisotropically. The viscosity of the fireball matter determines its ability to convert the initial spatial deformation into momentum anisotropies that can be measured in the final hadron spectra. A quantitatively precise empirical extraction of the QGP viscosity thus requires a good understanding of the initial fireball deformation. This deformation fluctuates from event to event, and so does the finally observed momentum anisotropy. We present a harmonic decomposition of the initial fluctuations in shape and orientation of the fireball and perform event-by-event (2+1)-dimensional ideal fluid dynamical simulations to extract the resulting fluctuations in the magnitude and direction of the corresponding harmonic components of the final anisotropic flow at midrapidity. The final harmonic flow coefficients are found to depend non-linearly on the initial harmonic eccentricity coefficients. We show that, on average, initial density fluctuations suppress the buildup of elliptic flow relative to what one obtains from a smooth initial profile of the same eccentricity, and discuss implications for the phenomenological extraction of the QGP shear viscosity from experimental elliptic flow data.

PACS numbers: 25.75.-q, 12.38.Mh, 25.75.Ld, 24.10.Nz

arXiv:1104.0650v3 [nucl-th] 21 Jul 2011

I. INTRODUCTION

In ultrarelativistic heavy-ion collision experiments, a fraction of the incoming kinetic energy is converted into new matter deposited in the collision zone. The distribution of this matter in the plane transverse to the colliding beams is inhomogeneous and fluctuates from collision to collision. At the collision energies available at the Relativistic Heavy Ion Collider (RHIC) and the Large Hadron Collider (LHC), the produced matter is sufficiently dense and strongly interacting that it quickly reaches a state of approximate local thermal equilibrium. Its subsequent evolution can thus be described by fluid dynamics until it eventually becomes too dilute and breaks apart. Hydrodynamic forces (i.e. pressure gradients) convert the inhomogeneities and deformations of its initial spatial density distribution into anisotropies of the final hydrodynamic flow. The latter can be extracted from the momentum distributions of the finally emitted particles. The efficiency with which the geometric deformation and fluctuating inhomogeneities in the initial density distribution are converted into final flow anisotropies is controlled by the viscosity of the expanding fluid. For a given source deformation, ideal fluid dynamics generates the largest flow anisotropy; it corresponds to the limit of zero mean free path and instantaneous thermalization, which allows for the largest possible collective response, via final state interactions, to irregularities in the geometric structure of the fireball [1]. Viscosity accounts for finite interaction cross sections and non-zero mean free paths which reduce the amount of flow anisotropy that can be generated from a given geometric deformation. In hydrodynamic language, viscous pressure components inhibit the development of flow anisotropies and tend to smoothen irregularities in the flow distribution. By measuring the flow anisotropies and relating them to the initial geometric deformations (as calculated from theoretical models for the collision geometry) one can, in principle, determine the fluid's viscosity experimentally [2–6].

Until recently, most of the attention has been focussed on elliptic flow $v_2 = \langle \cos(2\phi_p) \rangle$ and its relation to the spatial eccentricity $\varepsilon_x = \frac{\langle y^2 - x^2 \rangle}{\langle y^2 + x^2 \rangle} = \langle r^2 \cos(2\phi_s) \rangle / \langle r^2 \rangle$ (more precise definitions will be given in Sec. II) [2–12]. Event-by-event fluctuations in the initial state were only treated on average, by taking into account their effects on the average eccentricity of an ensemble of events [5, 6, 11–13] and then propagating a smooth initial density profile corresponding to that ensemble average hydrodynamically. In this way one can only compute the average elliptic flow, but not its fluctuations from event to event [14–16]. If one assumes that the elliptic flow is linearly proportional to the initial eccentricity, one can distribute the elliptic flow fluctuations around this average v_2 value in the same way as the initial eccentricity fluctuates around its average [17] and use this to predict flow fluctuations from eccentricity fluctuations [18]. This ignores, however, the recently discovered [19] fact that initial-state shape fluctuations of the collision region lead to event-by-event fluctuations not only of the elliptic deformation ε_x, but simultaneously of all higher-order harmonic eccentricity coefficients [20, 21], and that the simultaneous presence of several harmonic eccentricity coefficients can lead to hydrodynamic cross-talk between anisotropic flows of different harmonic order [20]. Without the possibility to hydrodynamically evolve fluctuating initial conditions event-by-event, the assumption of a linear dependence of v_2 on ε_x can thus not be rigorously tested.

Experimentally, anisotropic flow coefficients v_n are measured by analyzing multiparticle correlations in azimuthal angle around the beam axis [24]. Event-by-event flow fluctuations and additional non-flow correlations influence the elliptic flow v_2 derived from different such measures in different ways [22–25] and affect the magnitude of the extracted flow. This has serious implications

for the determination of the quark-gluon plasma shear viscosity from elliptic flow data [5, 6]: quantitatively trustworthy results require a detailed understanding of the spectrum of fluctuations of the anisotropic flow coefficients in the experimentally observed final state and its relation to the fluctuations of the corresponding moments of the initial eccentricity distributions that are believed to drive the flows measured by various different methods. In addition, widely held beliefs as to which moments of the initial eccentricity distribution are directly related to which moments of the final flow distribution [17, 21, 26] must be tested by generating the final states hydrodyamically event by event, i.e. separately for each fluctuating initial condition [20, 27–31]. These are the goals addressed in the present article. (For related work using non-hydrodynamic models for the transfer of initial eccentricities into final flows see [32].)

To generate fluctuating initial conditions we use Monte Carlo versions of the Glauber [33] and `fKLN` [34, 35] models, in the implementation by Hirano and Nara [11, 12]. After defining and compiling in Sec. II several different definitions of initial-state eccentricities and final-state harmonic flow coefficients, we explore in Sec. III the centrality dependence of the average ellipticity, triangularity and a few higher-order harmonic coefficients in their various incarnations found in the literature. In Sec. IV we use ideal event-by-event hydrodynamics[1] to analyze the correlations between final state flow anisotropies and their associated flow angles with the initial state eccentricity coefficients and their associated angles. We identify strong cross-talk between coefficients of different harmonic order, especially in peripheral collisions with strong elliptic flow. In Section V we compare the conversion efficiency of initial-state ellipticity and triangularity into final-state elliptic and triangular flow in single-shot and event-by-event hydrodynamics. We find significant differences and discuss their implications. We summarize our results in Section VI and discuss different radial weights for the eccentricity definitions in the Appendix.

II. DEFINITIONS

In this section we discuss different definitions for the harmonic flow and eccentricity coefficients and briefly describe the models used in computing the initial entropy and energy density profiles whose eccentricities are evaluated in Sec. III and which are evolved hydrodynamically in Sections IV and V.

A. Ellipticity

Usually known simply as "eccentricity", we define the "ellipticity" $\varepsilon \equiv \varepsilon_2$ of a given matter distribution in the transverse (x, y) plane in terms of its r^2-weighted second azimuthal moment [19, 26],

$$\varepsilon_2\, e^{i2\psi_2^{\rm PP}} = -\frac{\int dx\, dy\, r^2 e^{i2\phi}\, e(x,y)}{\int dx\, dy\, r^2\, e(x,y)}, \qquad (1)$$

where $x = r\cos\phi$, $y = r\sin\phi$. This formula assumes that the origin is the center of the distribution $e(x, y)$. In a Monte Carlo approach for generating the initial distribution $e(x, y)$ (see Sec. II D) this must be ensured by recentering each event before using Eq. (1). By default we characterize in Eq. (1) the matter distribution by its energy density $e(x, y)$ [36]. Since some authors (e.g. [11, 12]) prefer defining the source ellipticity in terms of its entropy density distribution $s(x, y)$, we compare in Sec. III B energy- and entropy-weighted ellipticities.

In Eq. (1), x and y are "reaction plane" (RP) coordinates: The reaction plane is the (x, z) plane, with z pointing along the beam and x pointing along the direction of the impact parameter $\boldsymbol{b}$ between the colliding nuclei. y is perpendicular to the reaction plane. Because of the minus sign on the r.h.s. of Eq. (1), the angle ψ_2 on the l.h.s. of Eq. (1) points in the direction of the minor axis of the corresponding ellipse. For an elliptically deformed Gaussian density distribution, this is the direction of the largest density gradient and thus of the largest hydrodynamic acceleration and also of the finally observed elliptic flow. The direction of this minor axis defines, together with the beam direction z, the "participant plane" (PP). It is tilted relative to the reaction plane by $\psi_2^{\rm PP}$. The label "participant" is motivated by the fact that the initial energy and entropy density distributions of the collision fireball reflect (more or less directly, depending on the model for secondary particle creation) the transverse distribution of the nucleons participating in the particle production process. The ellipticity ε_2 in Eq. (1) is correspondingly called *"participant eccentricity"* and also denoted as $\varepsilon_{\rm part}$.[2] It can be written as

$$\begin{aligned} \varepsilon_{\rm part} &\equiv \varepsilon_2 = |\varepsilon_2\, e^{i2\psi_2^{\rm PP}}| \\ &= \frac{\sqrt{\{r^2\cos(2\phi)\}+\{r^2\sin(2\phi)\}}}{\{r^2\}} \\ &= \frac{\sqrt{\{y^2{-}x^2\}^2+4\{xy\}^2}}{\{y^2{+}x^2\}}. \end{aligned} \qquad (2)$$

[1] For convenience we here use the longitudinally boost-invariant (2+1)-dimensional viscous hydrodynamic code `VISH2+1` [8] for zero viscosity, restricting our analysis to anisotropic transverse flow at midrapidity. This allows for easy later inclusion of viscous effects. A (3+1)-d viscous hydrodynamic code has recently become available [30], and a comparison between (2+1)-d and (3+1)-d viscous evolution near midrapidity is in progress [48].

[2] Traditionally $\varepsilon_{\rm part}$ is defined in terms of the transverse density of wounded nucleons, but since what matters for the subsequent hydrodynamic evolution is not the distribution of wounded nucleons themselves but of the matter generated by the wounded nucleons, we use the name $\varepsilon_{\rm part}$ for the ellipticity characterizing the thermalized matter.

Here $\{\dots\} = \int dx\, dy\, (\dots)\, e(x,y)$ defines the "event average" over the matter distribution $e(x,y)$ in a single collision event [23]. Equivalently, the participant eccentricity can be written as

$$\varepsilon_{\rm part} = \frac{\{y^2-x^2\}'}{\{y^2+x^2\}'} \tag{3}$$

where $\{\dots\}' = \int dx\, dy\, (\dots)\, e'(x,y)$ indicates the average over a rotated event with energy density $e'(x,y) = e\big(x\cos\psi_2^{\rm PP} - y\sin\psi_2^{\rm PP}, x\sin\psi_2^{\rm PP} + y\cos\psi_2^{\rm PP}\big)$ whose minor and major axes now align with x and y.

The event-average $\{\dots\}$ is to be distinguished from the the "ensemble average" $\langle\dots\rangle = \frac{1}{N}\sum_{n=1}^{N}\{\dots\}_n$ where N is the total number of events and $\{\dots\}_n$ is the event-average over the energy density $e_n(x,y)$ in event number n. The *average participant eccentricity* is thus defined as

$$\langle\varepsilon_{\rm part}\rangle = \frac{1}{N}\sum_{n=1}^{N}(\varepsilon_{\rm part})_n. \tag{4}$$

This differs from the *mean eccentricity* $\bar\varepsilon_{\rm part}$ of the average (recentered and rotated by $\psi_2^{\rm PP}$) energy density $\bar e'(x,y) = \frac{1}{N}\sum_{n=1}^{N} e'_n(x,y)$ which can be written in the following equivalent ways:

$$\bar\varepsilon_{\rm part} = \frac{\sqrt{\langle\{y^2-x^2\}\rangle^2 + 4\langle\{xy\}\rangle^2}}{\langle\{y^2+x^2\}\rangle} = \frac{\langle\{y^2-x^2\}'\rangle}{\langle\{y^2+x^2\}'\rangle}. \tag{5}$$

In contrast to (4), one here ensemble-averages over numerator and denominator separately before forming the ratio.

Nature performs heavy-ion collisions event by event, and hydrodynamic forces generate in each event an elliptic component v_2 of the anisotropic flow which is causally related to the specific initial ellipticity $\varepsilon_{\rm part}$ in that event. Theorists often do not compute the hydrodynamic evolution of the collision fireball event by event, but approximate Nature's procedure by generating from a superposition of many fluctuating initial conditions a single smooth initial distribution $\bar e(x,y)$ which they then evolve hydrodynamically in a "single shot", extracting the *mean elliptic flow* $\bar v_2$ corresponding to the *mean eccentricity* $\bar\varepsilon_{\rm part}$ of that averaged source distribution. Obviously, $\bar v_2$ is a deterministic consequence of $\bar\varepsilon_{\rm part}$ and does not fluctuate at all; it can not be measured experimentally. What can (at least in principle, although not easily in practice) be measured experimentally [16] is the *average elliptic flow* $\langle v_2\rangle$ of a large ensemble of collision events. This observable is conceptually more closely related to $\langle\varepsilon_{\rm part}\rangle$ than to $\bar\varepsilon_{\rm part}$; for an exactly linear hydrodynamic response $v_2 \sim \varepsilon_{\rm part}$, one has $\langle v_2\rangle/\langle\varepsilon_{\rm part}\rangle = \bar v_2/\bar\varepsilon_{\rm part}$ [17]. We will explore the differences between $\bar\varepsilon_{\rm part}$ and $\langle\varepsilon_{\rm part}\rangle$ and discuss consequences for the theoretically computed $\bar v_2$ as opposed to the measured [16] $\langle v_2\rangle$ in Secs. III A and V.

In addition to these "participant eccentricities" one can also define "reaction plane eccentricities". For a single event, the *reaction plane eccentricity* $\varepsilon_{\rm RP}$ is defined by

$$\varepsilon_{\rm RP} = \frac{\{y^2-x^2\}}{\{y^2+x^2\}} \tag{6}$$

in terms of an event-average over the (properly centered) energy density $e(x,y)$. The so-called *standard eccentricity* is defined as the analogous ratio of expectation values taken with a smooth average energy density $\bar e(x,y) = \frac{1}{N}\sum_{n=1}^{N} e_n(x,y)$ obtained by superimposing many events *without* rotating them from the participant to the reaction plane:

$$\varepsilon_s \equiv \bar\varepsilon_{\rm RP} = \frac{\langle\{y^2-x^2\}\rangle}{\langle\{y^2+x^2\}\rangle}. \tag{7}$$

In other words, the standard eccentricity is the *mean reaction plane eccentricity*. In contrast, the *average reaction plane eccentricity* is defined by

$$\langle\varepsilon_{\rm RP}\rangle = \left\langle\frac{\{y^2-x^2\}}{\{y^2+x^2\}}\right\rangle. \tag{8}$$

Contrary to what the reader may have been led to believe by our remarks above, experiments do *not* directly measure the average elliptic flow $\langle v_2\rangle$ (which for linear $v_2 \sim \varepsilon_{\rm part}$ would be directly related to the average participant eccentricity $\langle\varepsilon_{\rm part}\rangle$ (3)). Instead they measure quantities such as $v_2\{\rm EP\}$, $v_2\{2\}$, and $v_2\{4\}$ that, even if so-called non-flow contributions could be completely ignored, are affected by event-by-event v_2-fluctuations and thus differ from $\langle v_2\rangle$. $\langle v_2\rangle$ can be reconstructed from the experimental measurements with some additional assumptions [16] which on the surface look harmless but should be further tested. Motivated by the hypothesis of linear hydrodynamic response, $v_2 \sim \varepsilon_{\rm part}$, these v_2 measures motivate the definition of corresponding ellipticity measures [17], the so-called $2^{\rm nd}$ and $4^{\rm th}$ order cumulants:

$$\varepsilon\{2\} = \sqrt{\langle\varepsilon_{\rm part}^2\rangle} \tag{9}$$

and

$$\varepsilon\{4\} = \big(\langle\varepsilon_{\rm part}^2\rangle^2 - (\langle\varepsilon_{\rm part}^4\rangle - \langle\varepsilon_{\rm part}^2\rangle^2)\big)^{1/4}. \tag{10}$$

Note that the last expression involves the difference of two positive definite quantities which itself does not need to be positive definite. If fluctuations get large, the expression under the fourth root can become negative, leaving $\varepsilon\{4\}$ undefined. We will see that this can happen in the most central and the most peripheral centrality bins.

It was shown in [22] that in the MC-Glauber model the real and imaginary parts of the complex ellipticity defined by Eq. (1), with the wounded nucleon density as weight function on the r.h.s., both have approximately Gaussian fluctuations, with equal widths σ_ε. If this is the case, the magnitude ε_2 of this ellipticity exhibits fluctuations of

Bessel-Gaussian type[3] [37], leading to the identity [22]

$$\varepsilon\{4\} = \langle\varepsilon_{\rm RP}\rangle. \tag{11}$$

For sufficiently large average ellipticities $\langle\varepsilon_2\rangle$ (i.e. sufficiently large impact parameters) one may hope to be able to ignore the restriction that ε_2 can never fluctuate to negative values, and correspondingly assume the ε_2 exhibits Gaussian (instead of Bessel-Gaussian) fluctuations. In this case one has [22]

$$\begin{aligned}\varepsilon\{2\}^2 &= \langle\varepsilon_{\rm part}\rangle^2 + \sigma_\varepsilon^2, \\ \varepsilon\{4\}^2 &= \sqrt{(\langle\varepsilon_{\rm part}\rangle^2 - \sigma_\varepsilon^2)^2 - 2\sigma_\varepsilon^4},\end{aligned} \tag{12}$$

from which it follows that $\langle\varepsilon_2 = \varepsilon_{\rm part}\rangle^4$ is the arithmetic mean of $\varepsilon\{2\}^4$ and $\varepsilon\{4\}^4$:

$$\frac{\varepsilon\{2\}^4 + \varepsilon\{4\}^4}{2\langle\varepsilon_{\rm part}\rangle^4} = 1. \tag{13}$$

We will use Eqs. (11) and (13) (which hold irrespective of the fluctuation width σ_ε) in Sec. III A, and their analogues for the elliptic flow v_2 in Sec. V C, to test the assumptions of Bessel-Gaussian and Gaussian fluctuations of the event-by-event ellipticity and elliptic flow fluctuations in the Monte Carlo Glauber (MC-Glauber) and Monte Carlo fKLN (MC-KLN) models.

If the hydrodynamic response were indeed linear, $v_2 \sim \varepsilon_{\rm part}$, and non-flow effects could be ignored, the following identities would hold:

$$\frac{\langle v_2\rangle}{\langle\varepsilon_{\rm part}\rangle} = \frac{\bar{v}_2}{\bar{\varepsilon}_{\rm part}} = \frac{v_2\{2\}}{\varepsilon\{2\}} = \frac{v_2\{4\}}{\varepsilon\{4\}}. \tag{14}$$

To test these theoretically one needs event-by-event hydrodynamics which is the only possibility to properly account for event-by-event flow fluctuations. In the past, event-by-event hydrodynamical evolution of fluctuating initial conditions has been technologically out of reach. Comparisons between theory and experiment have been based on "single-shot hydrodynamic evolution" which propagates a smooth initial profile obtained by either using the so-called optical versions of the Glauber and fKLN models or averaging over many fluctuating initial profiles from their Monte Carlo versions (MC-Glauber and MC-KLN, respectively). Assuming linear hydrodynamic response, one can still compare the theoretically computed $\langle v_2\rangle$ with the experimentally measured $v_2\{2\}$ or $v_2\{4\}$ if one normalizes the former by $\langle\varepsilon_{\rm part}\rangle$ and the latter by $\varepsilon\{2\}$ or $\varepsilon\{4\}$, respectively, calculated *from the same initial state model* [5, 6]. In this context the identity $\varepsilon\{4\} = \langle\varepsilon_{\rm RP}\rangle$ (which holds if the ellipticity fluctuations are Gaussian) becomes particularly useful because it suggests that the measured $v_2\{4\}$ can be directly compared with a single-shot hydrodynamic v_2 obtained from a smooth reaction-plane averaged initial density of ellipticity $\langle\varepsilon_{\rm RP}\rangle$, without any corrections for flow fluctuations. Even better, $v_2\{4\}$ can be shown to be completely free of two-particle non-flow contributions [17, 22]. These arguments have been used in [12] and provide a strong motivation for us to test the underlying assumptions (Gaussian ellipticity fluctuations and linear hydrodynamic elliptic flow response) in the present work.

We close this subsection by recalling the expression for the participant plane angle of a given event (see e.g. [23])

$$\psi_2^{\rm PP} = \frac{1}{2}\tan^{-1}\left(\frac{2\{xy\}}{\{y^2 - x^2\}}\right) \tag{15}$$

and for its transverse area

$$S = \pi\sqrt{\{x^2\}'\{y^2\}'}. \tag{16}$$

Both expressions assume that the events are properly centered at the origin.

B. Higher order eccentricity coefficients

The definition (1) can be generalized to higher harmonic eccentricity coefficients [19, 26]:

$$\varepsilon_n\, e^{in\psi_n^{\rm PP}} = -\frac{\int dx\, dy\, r^2 e^{in\phi}\, e(x,y)}{\int dx\, dy\, r^2\, e(x,y)}. \tag{17}$$

Alternatively one can use r^n instead of r^2 as radial weight on the right hand side [20]:

$$\varepsilon_n'\, e^{in\psi_n'^{\rm PP}} = -\frac{\int dx\, dy\, r^n e^{in\phi}\, e(x,y)}{\int dx\, dy\, r^n\, e(x,y)}. \tag{18}$$

Still another variant uses the entropy density $s(x,y)$ instead of the energy density $e(x,y)$ as weight function:

$$\varepsilon_n(s)\, e^{in\psi_n^{\rm PP}(s)} = -\frac{\int dx\, dy\, r^2 e^{in\phi}\, s(x,y)}{\int dx\, dy\, r^2\, s(x,y)}, \tag{19}$$

$$\varepsilon_n'(s)\, e^{in\psi_n'^{\rm PP}(s)} = -\frac{\int dx\, dy\, r^n e^{in\phi}\, s(x,y)}{\int dx\, dy\, r^n\, s(x,y)}. \tag{20}$$

We note that the r^2-weighted eccentricity coefficients ε_n fall off faster with increasing harmonic order n than the r^n-weighted eccentricities ε_n' (see Appendix). Also, as in (1), the minus sign in Eqs. (17)-(20) guarantees that, for a Gaussian density distribution that has only $n^{\rm th}$-order eccentricity ε_n, the angle $\psi_n^{\rm PP}$ points in the direction of the steepest density gradient, and thus in the direction of the corresponding hydrodynamically generated $n^{\rm th}$-order harmonic flow v_n (see next subsection). It can be written as $-1 = e^{-in(\pi/n)}$ and amounts to a rotation of $\psi_n^{\rm PP}$ by π/n. For example, if the profile is square-shaped, $\psi_4^{\rm PP}$ points to the sides instead of its corners.

[3] This takes into account that ε_2 can never fluctuate to negative values.

A complete characterization of the fluctuating initial density profile, that captures all aspects of the location of "hot-spots" and their gradients, uses an expansion of the initial (energy or entropy) density profile in terms of cumulants [38]. We will postpone their discussion to a future analysis.

As stated before, we will use the energy density as the default weight function; in cases of possible ambiguity, we will use the notations $\varepsilon_n(e)$, $\varepsilon_n(s)$ etc. to distinguish between energy and entropy density weighted eccentricity coefficients and angles. Eccentricities ε without harmonic index n denote ellipicities (i.e. in the absence of n, $n=2$ is implied).

The coefficients ε_n and angles $\psi_n^{\rm PP}$ define the eccentricies and angles of the matter distribution in the participant plane. We note that the participant plane angles $\psi_n^{\rm PP}$ associated with eccentricity coefficients of different harmonic order n do not, in general, agree (see Sec. IV A). We will not study higher harmonic generalizations of the reaction-plane ellipticity (6).

C. Harmonic flow coefficients

We charaterize the finally observed momentum distribution $dN/(dy\,p_T dp_T\,d\phi_p)$ by "harmonic flow coefficients" constructed in analogy to Eq. (17), but without the extra minus sign:

$$v_n(y,p_T)\,e^{in\psi_n^{\rm EP}(y,p_T)} = \frac{\int d\phi_p\, e^{in\phi_p}\,\frac{dN}{dy\,p_T dp_T\,d\phi_p}}{\frac{dN}{dy\,p_T dp_T}}, \quad (21)$$

$$v_n(y)\,e^{in\psi_n^{\rm EP}(y)} = \frac{\int p_T dp_T\,d\phi_p\, e^{in\phi_p}\,\frac{dN}{dy\,p_T dp_T\,d\phi_p}}{\frac{dN}{dy}}. \quad (22)$$

In boost-invariant hydrodynamics they are rapidity-independent, so we drop the argument y and keep in mind that we should only compare with midrapidity data at $y=0$ where the assumption of boost-invariant longitudinal expansion is most justified. The spectra $\frac{dN}{dy\,p_T dp_T\,d\phi_p}$ are computed from the hydrodynamic output with the Cooper-Frye prescription [39] along an isothermal kinetic decoupling surface of temperature $T_{\rm dec}=140\,$MeV. Equation (21) defines the p_T-differential harmonic flow $v_n(p_T)$ and flow angle $\psi_n^{\rm EP}(p_T)$, whereas Eq. (22) gives their p_T-integrated values v_n and $\psi_n^{\rm EP}$. The orientation of the final momentum distribution defines the "event plane", indicated by superscript EP. Again, different harmonic flows are usually associated with differently oriented event planes. The first three harmonic flow coefficients are the directed flow (v_1), elliptic flow (v_2), and triangular flow (v_3).

D. Initial-state models

We use Monte Carlo versions [11, 12] of the Glauber [33] and `fKLN` [35] models to generate fluctuating initial conditions for the entropy density in 200 A GeV Au+Au collisions. For the MC-Glauber model we assume a two-component (soft+hard) model with a small hard fraction ($\delta=0.14$ [11]); we also use a Woods-Saxon profile for the distribution of nucleon centers whose radius and surface thickness parameters have been corrected for the finite nucleon size [11]. The resulting entropy density profile is normalized to the final charged hadron multiplicity density $dN_{\rm ch}/dy$ in central collisions; after this normalization, the centrality dependence of the initial entropy production is fixed by the model (MC-Glauber or MC-KLN). To convert the initial entropy density to energy density, we use the equation of state (EOS) s95p-PCE which matches Lattice QCD data at high temperatures to a chemically frozen hadron resonance gas at low temperatures [40, 41], using $T_{\rm chem}=165\,$MeV as chemical freeze-out temperature.

TABLE I: Centrality table for Au+Au at 200 A GeV [11].

centrality	$b_{\rm min}$(fm)	$b_{\rm max}$(fm)	$\bar{b}$ (fm)	$\bar{N}_{\rm part}$
0-5%	0.0	3.3	2.2	352.2
5-10%	3.3	4.7	4.04	294.7
10-15%	4.7	5.8	5.27	245.6
15-20%	5.8	6.7	6.26	204.2
20-30%	6.7	8.2	7.48	154.5
30-40%	8.2	9.4	8.81	103.8
40-50%	9.4	10.6	10.01	64.9
50-60%	10.6	11.6	11.11	36.6
60-70%	11.6	12.5	12.06	18.8
70-80%	12.5	13.4	12.96	7.5
80-90%	13.4	14.3	13.85	4.4

In the following we compute harmonic eccentricity and flow coefficients as functions of impact parameter b and collision centrality (%). The centrality classes are defined in terms of percentages of the total inelastic cross section, calculated from the distribution of the number of wounded nucleons $dN_{\rm event}/dN_{\rm part}$ in the optical Glauber model (i.e. without accounting for fluctuations in $N_{\rm part}$ at given impact parameter). Each centrality class is thus characterized by a range of impact parameters $b_{\rm min} < b < b_{\rm max}$ and an average value $\bar{b}$, together with a mean number of wounded nucleons $\bar{N}_{\rm part}$. They are listed in Table I [11].

E. Averaging procedures for the initial profiles

In this work we compare results obtained from an event-by-event hydrodynamical evolution of fluctuating initial conditions with the traditional method of "single-shot" hydrodynamic evolution, where one first averages over many fluctuating initial profiles to obtain a smooth average profile, and then evolves this smooth profile hy-

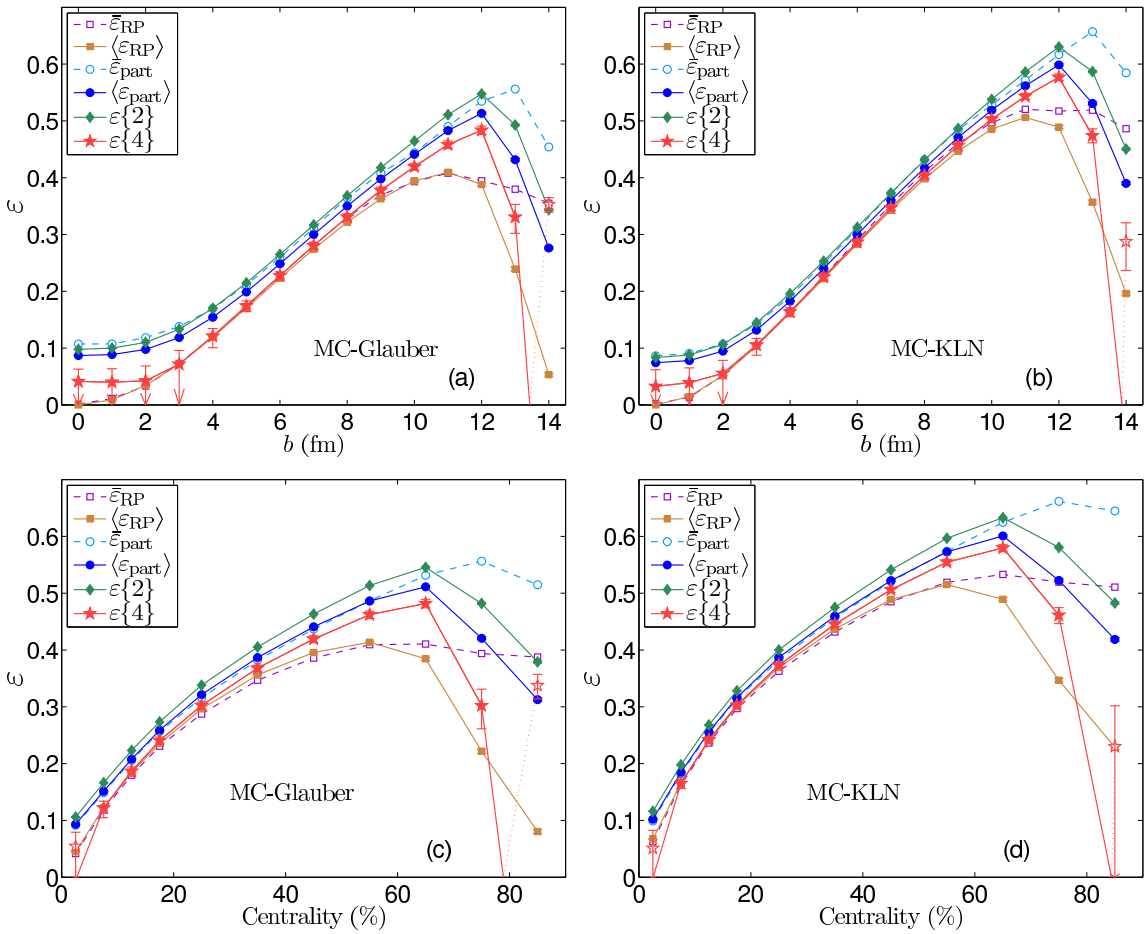


FIG. 1: (Color online) Different ellipticities as a function of impact parameter (top row) or collision centrality (bottom row), for the MC-Glauber (panels (a) and (c)) and the MC-KLN model (panels (b) and (d)). Panels (a,b) show e-weighted, panels (c,d) show s-weighted ellipticities. (See Figs. 3, 4 below for a direct comparison between e- and s-weighted eccentricities.) Open stars indicate negative values for $\varepsilon\{4\}^4$.

drodynamically. The question addressed in this comparison is to what extent the average harmonic flow coefficients from event-by-event hydrodynamics can be faithfully represented by the harmonic flow coefficients extracted (at much lower numerical expense) from the hydrodynamic evolution of an "average event".

Taking the initial density profiles from the Monte Carlo generator and superimposing them directly without additional manipulations generates a "reaction plane averaged" profile with ellipticity $\bar{\varepsilon}_{\rm RP}$ (Eq. (7)). After recentering each event to the origin of the x-y-plane, we can compute event by event the reaction and participant plane ellipticities (Eqs. (6) and (2,3)) and evaluate their ensemble averages (8) and (4), respectively. To generate a smooth average profile with ellipticity $\bar{\varepsilon}_{\rm part}$ (Eq. 5) we rotate each recentered event by the angle $\psi_2^{\rm PP}(e)$ ($\psi_2^{\rm PP}(s)$) if we want to determine the eccentricity of the average energy (entropy) density. For the calculation of entropy-weighted average eccentricities we perform any ensemble average first and convert the result to energy density later; in this case all events are rotated by their $\psi_2^{\rm PP}(s)$ angles. For energy-weighted ensemble averages we convert s to e in each event first, rotate by $\psi_2^{\rm PP}(e)$ and perform the ensemble average last. Other sequences or mixtures of these steps are technically possible but physically not meaningful. Note that the processes of computing the energy density from the entropy density via the EOS and of averaging the event profiles do not commute: The energy density obtained via the EOS from the ensemble-averaged entropy density profile is not the same as the ensemble-averaged energy density where the EOS is used in each event to convert s to e.

III. ECCENTRICITIES

A. Centrality dependence of different ellipticities

Fig. 1 shows a comparison between the different ellipticities defined in Sec. II A, as functions of the impact parameter b in panels (a) and (b) and as functions of collision centrality (as defined in Sec II D) in panels (c) and

(d). For panels (a) and (b) we generated 10,000 initial profiles for each impact parameter (except for $b=0$, 1, and 2 fm for which we generated 30,000 events each); for panels (c) and (d) we averaged over 10,000 profiles for each centrality bin. Within the centrality bins, the impact parameters were sampled between $b_{\rm min}$ and $b_{\rm max}$ with $b\,db$ weight. Compared to panels (a) and (b), this leads to additional ellipticity fluctuations related to the fluctuating impact parameter, whereas in Fig. 1a,b only $N_{\rm part}$ fluctuations at fixed b contribute.

As discussed in Sec. II A, Eq. (10), $\varepsilon\{4\}^4$ can become negative when fluctuations grow large. Whenever this happens, we replace $\varepsilon\{4\}$ by $\sqrt[4]{|\varepsilon\{4\}^4|}$ and indicate this by an open star in Fig. 1 (connected by dotted lines to other points in the graph). One sees that $\varepsilon\{4\}^4$ has a tendency to turn negative in the most peripheral collisions. In very central collisions $\varepsilon\{4\}^4$ becomes very small, with central values that can have either sign depending on whether we keep the impact parameter fixed (Figs. 1a,b) or average over events with different impact parameters in a given centrality bin (see the 0−5% centrality values in Figs. 1c,d). Statistical errors are large, however, and within errors $\varepsilon\{4\}^4$ is compatible with zero for impact parameters $b<3$ fm, i.e. in the most central (0−5% centrality) collisions. We indicate this by open-ended error bars for $\sqrt[4]{|\varepsilon\{4\}^4|}$, pointing from its upper limit all the way to zero.

Comparing panels (a,c) for the MC-Glauber model with panels (b,d) for the MC-KLN model we see great similarities in shape, but systematic differences in magnitude of the ellipticities. The ratio of the MC-KLN and MC-Glauber ellipticities is shown in Fig. 2. Except for the most central and most peripheral collisions, the MC-KLN ellipticities exceed the MC-Glauber ones by an approximately constant factor of around 1.2. Please note

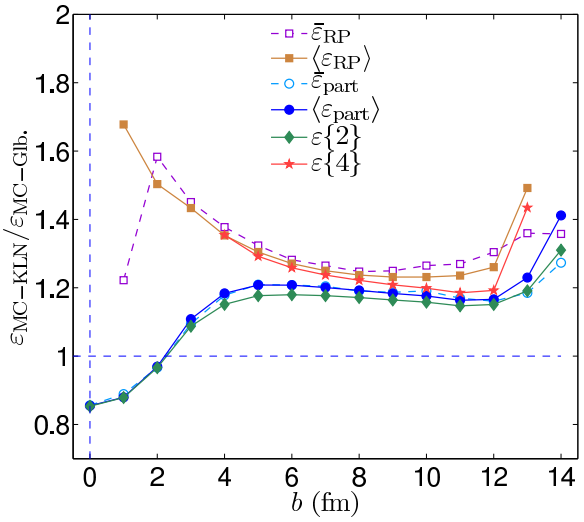


FIG. 2: (Color online) Impact parameter dependence of the ratio of ellipticities obtained from the MC-KLN and MC-Glauber models as shown in Figs. 1a,b.

the difference in the ratios for the reaction plane and participant eccentricities at small b. (The point for $\bar{\varepsilon}_{\rm RP}$ at $b=1$ fm is obtained from a ratio of very small numbers and probably not statistically robust – we had only 30,000 events to determine the ensemble-averaged density profile.) For the $\varepsilon\{4\}$ ratio we dropped all points where the statistical error for $\varepsilon\{4\}^4$ extended into the region of negative values for either the MC-Glauber or MC-KLN model.

Figure 1 shows that, for central and mid-peripheral collisions, the ensemble-averaged participant and reaction plane eccentricities $\langle\varepsilon_{\rm part}\rangle$ and $\langle\varepsilon_{\rm RP}\rangle$ agree very well with the mean eccentricities $\bar{\varepsilon}_{\rm part}$ and $\bar{\varepsilon}_{\rm RP}$ of the corresponding ensemble-averaged profiles. For strongly peripheral collisions ($b\gtrsim 10$ fm), however, the average of the ratio (Eqs. (3,4,8)) differs strongly from the ratio of averages (Eqs. (5,7)), indicating strong event-by-event fluctuations. We note that in very peripheral collisions the average event ellipticity drops quickly with increasing b while the ellipticity of the average profile remains large; single-shot hydrodynamic calculations based on a smooth average initial profile thus overestimate the effective initial source ellipticity and produce more elliptic flow than expected from event-by-event hydrodynamic evolution of individual peripheral events. Still, as first emphasized in [6], the calculated v_2 from single-shot hydrodynamics decreases steeply at large collision centralities [12, 42–44], due to the decreasing fireball lifetime, which contrasts with the initially reported experimentally observed behaviour [45, 46], but agrees qualitatively with a recent reanalysis [47] where non-flow effects have been largely eliminated and/or corrected for. We do point out that our Monte-Carlo simulations do not include fluctuations in the amount of entropy generated per nucleon-nucleon collision [20]; these could have important effects on the ellipticities in very peripheral collisions.

Comparing the curves for $\langle\varepsilon_{\rm part}\rangle$, $\varepsilon\{2\}$ and $\varepsilon\{4\}$ in Fig. 1 we see that (as is manifest in the Gaussian model analysis in Eq. (12)) $\varepsilon\{2\}$ receives a positive and $\varepsilon\{4\}$ receives a negative contribution from event-by-event ellipticity fluctuations. In Fig. 3 we check, as a function of impact parameter, the validity of the identities (11) and (13) which follow from Bessel-Gaussian and Gaussian $\varepsilon_{\rm part}$ distributions, respectively. We see that both hold with good accuracy in the mid-centrality range ($b\lesssim 10$ fm for Eq. (11), $5\lesssim b\lesssim 11$ fm for Eq. (13)) but break down in the most peripheral collisions. Both the Gaussian and Bessel-Gaussian hypotheses work slightly better for the MC-KLN than for the MC-Glauber model. Consistent with the analysis in Ref. [22], the Gaussian fluctuation hypothesis for $\varepsilon_{\rm part}$ breaks down at small impact parameters whereas (as theoretically expected [22]) the Bessel-Gaussian hypothesis appears to continue to hold, although we are unable to make this statement with statistical confidence. (For the ratio $(\varepsilon\{4\}-\langle\varepsilon_{\rm RP}\rangle)/(\varepsilon\{4\}+\langle\varepsilon_{\rm RP}\rangle)$ we again dropped all points for which the error band for $\varepsilon\{4\}^4$ reaches into negative territory.)

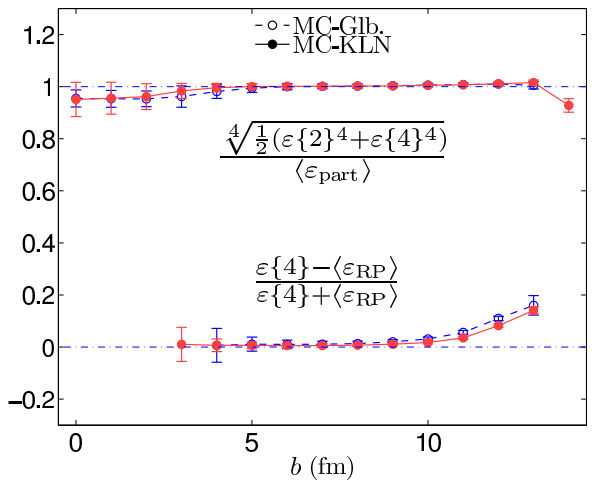


FIG. 3: (Color online) Checks of the assumption of Gaussian and Bessel-Gaussian fluctuations for $\varepsilon_{\rm part}$ (see text for discussion).

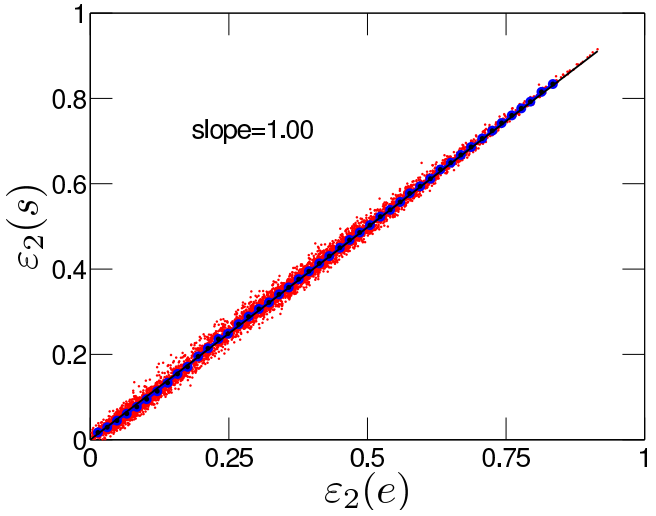


FIG. 4: (Color online) $\varepsilon_{\rm part}(e)$ vs. $\varepsilon_{\rm part}(s)$ for 6000 initial profiles from the MC-KLN model (1000 each for $b=0$, 0−5%, 15−20%, 20−30%, 30−40%, and 50−60% centrality).

The assumption of Gaussian fluctuations of the real and imaginary parts of the complex ellipticity (1) is often used to argue that the average reaction-plane ellipticity $\langle\varepsilon_{\rm RP}\rangle$ can serve as a proxy for $\varepsilon\{4\}$ (see Eq. (11)), and that therefore reaction-plane averaged initial density profiles can be used in single-shot hydrodynamics (which ignores event-by-event fluctuations) to simulate the experimentally measured $v_2\{4\}$ values. Fig. 1 and the bottom curves in Fig. 3 show that $v_2\{4\}$ values obtained from single-shot hydrodynamic simulations with reaction-plane averaged initial conditions [12, 43] should not be trusted quantitatively for centralities $> 40\%$.

To summarize this subsection, all the simplifying assumptions that allow to focus attention on the three quantities $\langle\varepsilon_{\rm part}\rangle$, $\varepsilon\{2\}$ and $\varepsilon\{4\}$ only (by substituting $\langle\varepsilon_{\rm part}\rangle$ for $\bar{\varepsilon}_{\rm part}$ and $\varepsilon\{4\}$ for $\bar{\varepsilon}_{\rm RP}$ or $\langle\varepsilon_{\rm RP}\rangle$) hold well for central to mid-central collisions ($\lesssim 40\%$ centrality) but break down for peripheral collisions. For $> 40\%$ centrality there exists no substitute for event-by-event hydrodynamics if one aims for quantitative precision in the comparison with experimental data, since the latter are strongly affected by non-Gaussian event-by-event fluctuations at those centralities.

B. Ellipticities with different weight functions

Figure 4 shows a comparison between the energy- and entropy-weighted ellipticities of the initial profiles generated with the MC-KLN model, on an event-by-event basis. The scatter plot is based on 6000 events, 1000 each for $b = 0$ and for the following finite-width centrality bins: 0−5%, 15−20%, 20−30%, 30−40%, and 50−60%. This is not a realistic mix in the experimental sense, but permits us to explore the full range from very small to very large event ellipticities. The blue dots in Fig. 4 represent bin averages, and the solid black line is a linear fit through the origin. The fitted slope is 1.00, the scatter plot is seen to be tightly clustered around this fitted line, and only at small ellipticities $\varepsilon_2 < 20\%$ the e-weighted values are seen to be slightly larger on average than their s-weighted counterparts (see also Fig. 5a below).

C. Higher order harmonics

In Figs. 5a-d we compare the centrality dependences of the ensemble-averaged second to fifth harmonic eccentricity coefficients (energy- and entropy-weighted) from the MC-Glauber and MC-KLN models. The contour plots give a visual impression of the degree of deformation corresponding to the (larger) MC-KLN eccentricities, assuming (for illustration) the absence of any other eccentricity coefficients than the one shown in the particular panel.

First, one observes very little difference between the eccentricities of the entropy and energy density profiles, except for very central collisions ($b \lesssim 5$ fm for the MC-Glauber, $b \lesssim 3$ fm for the MC-KLN model) where the energy-weighted eccentricities lie systematically somewhat above the entropy-weighted ones (for all orders n studied here). The difference between s- and e-weighted eccentricities at small b is bigger in the MC-Glauber than in the MC-KLN model.

Next, one notes the significantly larger ellipticities and quadrangularities of the MC-KLN distributions compared to those from the MC-Glauber model, for all but the most central collisions. These are driven by geometry, i.e. by the almond-shaped deformation of the nuclear overlap zone in non-central collisions, which in the KLN-model is more eccentric than in the Glauber model. The

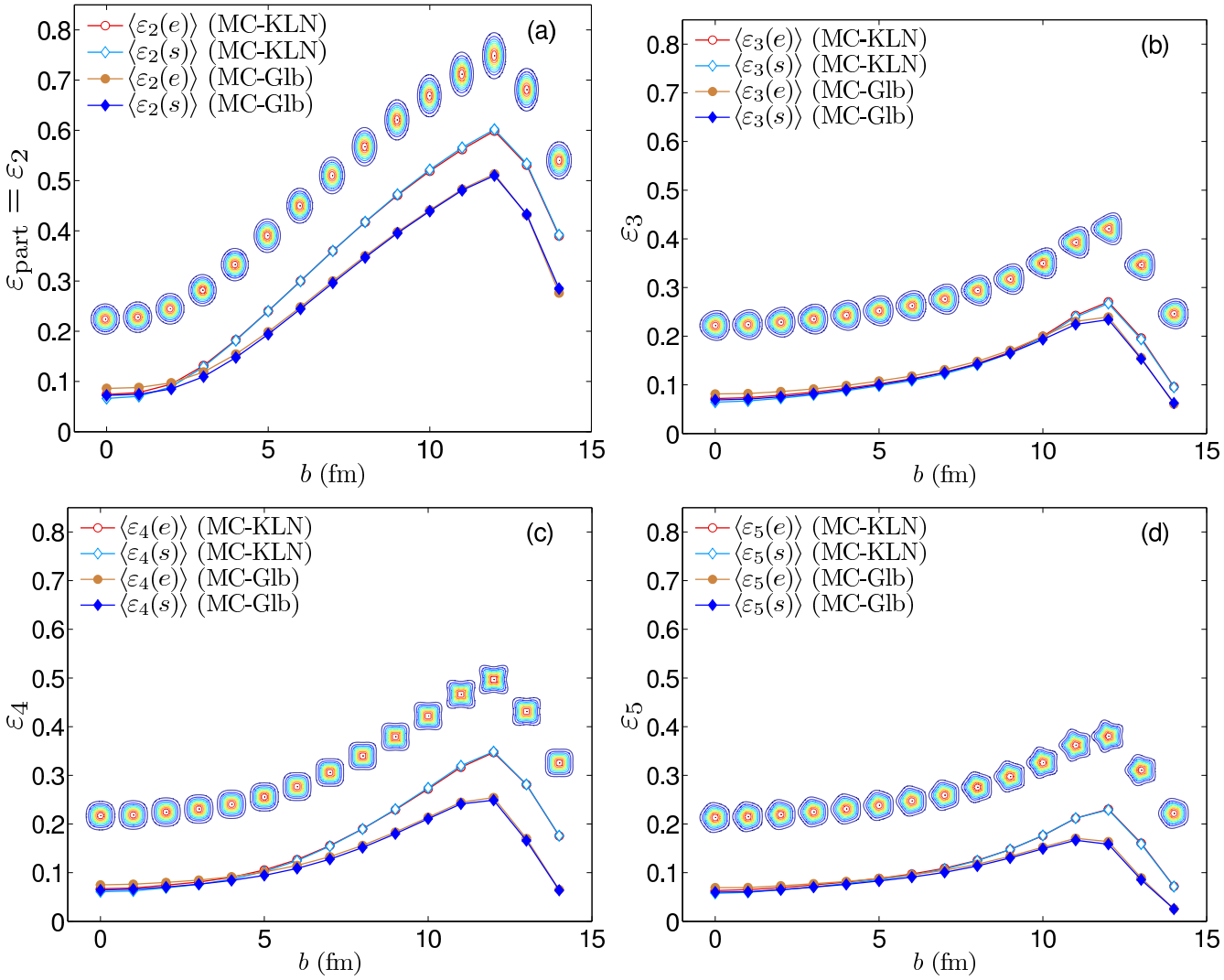


FIG. 5: (Color online) Harmonic eccentricity coefficients $\varepsilon_2 = \varepsilon_{\rm part}$ (a), ε_3 (b), ε_4 (c) and ε_4 (d) as functions of impact parameter, calculated from the MC-Glauber (filled symbols, solid lines) and MC-KLN models (open symbols, dashed lines), using the energy density (circles) or entropy density (triangles) as weight function. The contour plots illustrate deformed Gaussian profiles $e(r,\phi) = e_0 \exp\left[-\frac{r^2}{2\rho^2}\left(1+\varepsilon_n \cos(n\phi)\right)\right]$, with eccentricity $\varepsilon_n(e)$ taken from the MC-KLN model at the corrsponding impact parameter.

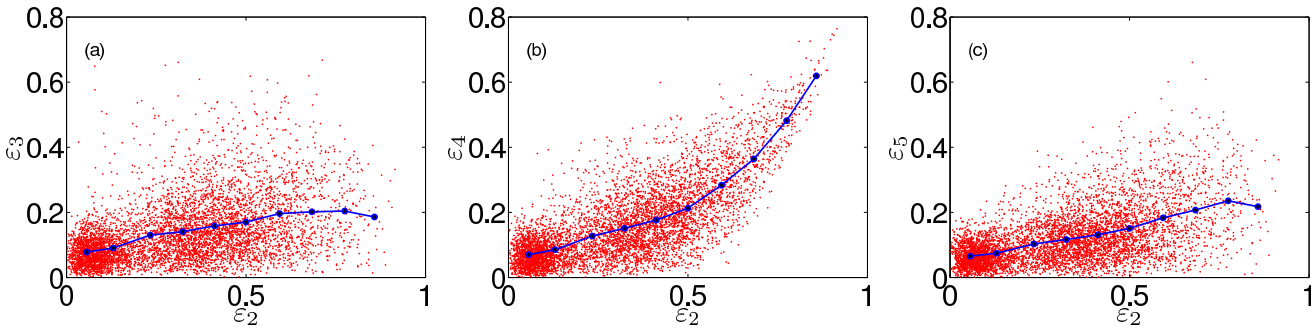


FIG. 6: (Color online) Scatter plots illustrating the event-by-event correlation of ε_3 (a), ε_4 (b), and ε_5 (c) with the fireball ellipticity $\varepsilon_2 = \varepsilon_{\rm part}$, for the same set of 6000 event profiles analyzed in Fig. 4. The blue dots connected by a line indicate ε_2-bin averages, to guide the eye.

third and fifth order harmonics, which are entirely due to fluctuations (and whose associated angles $\psi_n^{\rm PP}$ are therefore completely uncorrelated to the reaction plane – see Ref. [20] and discussion below), show remarkably similar eccentricity values in the two initialization models, except for the most peripheral events. Comparing the viscous suppression of elliptic and triangular flow thus should allow to distinguish experimentally between the MC-Glauber and MC-KLN models [49].

Third, in central collisions all four eccentricity coefficients are roughly of the same size. In peripheral collisions, the fluctuation-dominated eccentricity coefficients (ε_3 and ε_5) are generically smaller than the geometry-dominated ones (ε_2, but also to some extent ε_4).[4] This is less obvious when one defines the higher order eccentricities with r^n instead of r^2 weight [20], which tends to increase the values of the higher harmonics in peripheral collisions.

Even with "only" an r^2 weight, ε_4 and ε_5 are seen to become large enough around $b \sim 10 - 13\,$fm that, if collective acceleration happens predominantly in the directions of steepest descent of the density profile, one has to expect cross-currents in the developing anisotropic flow patterns. These can lead to destructive interference and a correspondingly reduced efficiency of converting $n^{\rm th}$-order eccentricities ε_n into $n^{\rm th}$-order harmonic flows v_n [26]. In realistic situations this issue is exacerbated by the simultaneous presence of *several* large eccentricity components ε_n, which is expected to lead to a strongly non-diagonal and probably non-linear response matrix relating v_n to ε_n [20]. This will be discussed in Sec. IV.

D. Eccentricity correlations

It is reasonable to ask whether and how the different harmonic eccentricity coefficients ε_n are correlated with each other. Figure 6 shows scatter plots of the correlations between $\varepsilon_{3,4,5}$ and the ellipticity ε_2 which, for large ε_2 values, is dominated by geometric overlap effects. We note that, according to the definition (17), all eccentricity coefficients are positive definite, $\varepsilon_n \geq 0$. Keeping this in mind, Figs. 6a,c show that ε_3 and ε_5 are uncorrelated with the fireball ellipticity; the slight growth of $\langle\varepsilon_{3,5}\rangle$ with increasing ε_2 is related to the growth of the variances of their distributions in more peripheral collisions.

In contrast, the quadrangularity ε_4 shows a clear positive correlation with the ellipticity, see Fig. 6b. It is of geometrical origin: it reflects the football or almond shape of the overlap zone in non-central collisions which is a little sharper than a pure $\cos(2\phi)$ deformation. This is corroborated by the angle $\psi_4^{\rm PP}$ shown in Fig. 7a which, on average, points 45° relative to $\psi_2^{\rm PP}$ (which again points in x-direction). This means that the quadrangular component of the initial fireball definition is oriented like a diamond, with its corners on the x and y axes. Superimposing it on a pure $\cos(2\phi)$ deformation leads to a somewhat sharper shape of the density distribution.

[4] We checked that the centrality dependences of the ratios $\varepsilon_n/\varepsilon_3$ agree qualitatively, but not quantitatively with Fig. 3 in Ref. [21]. We suspect that the differences, which are larger for the MC-Glauber than the MC-KLN model, are due to somewhat different Woods-Saxon and (in the MC-Glauber case) fluctuation size parameters used in Ref. [21].

IV. EVENT-BY-EVENT HYDRODYNAMICS AND FLOW FLUCTUATIONS

In this section we analyze the results from ideal fluid event-by-event hydrodynamic evolution of the fluctuating initial profiles studied in the previous section. We focus on the anisotropic flow coefficients v_n, their relationship to the initial eccentricity coefficients ε_n, and the correlation between the $n^{\rm th}$-order flow angles $\psi_n^{\rm EP}$ and the corresponding $n^{\rm th}$-order participant-plane angles $\psi_n^{\rm PP}$ associated with ε_n.

A. Correlations between participant plane, event plane, and reaction plane

One of the key characteristics of fluid dynamics is its ability to transform initial geometric deformation into a deformation of the final momentum distribution, via collective flow. This happens through spatially anisotropic hydrodynamic forces (i.e. pressure gradients) which cause anisotropic acceleration of the fluid. As a result, correlations between participant and event planes are expected: The angle $\psi_n^{\rm PP}$ points in the direction of the largest pressure gradient associated with the $n^{\rm th}$ harmonic component of the spatial deformation of the initial density distribution, while $\psi_n^{\rm EP}$ points into the direction where the $n^{\rm th}$ harmonic component of the final collective flow is largest. Without interference between harmonics of different order, we would thus expect $\psi_n^{\rm PP}$ and $\psi_n^{\rm EP}$ to point, on average and up to event-by-event fluctuations, in the same direction.

In Figs. 7a,b we show the distribution of participant and event plane angles, associated with the $n^{\rm th}$-order eccentricities and harmonic flows, relative to the x-z reaction plane. The analysis uses the same 6000 events as before. In panel (a) we see that $\psi_{3,5}^{\rm PP}$ are completely uncorrelated with the reaction plane [20], as expected from the fact that the corresponding eccentricities are entirely fluctuation-driven, without contribution from the collision geometry. Panel (b) shows that the same holds true for $\psi_{3,5}^{\rm EP}$, which is (at least superficially) consistent with the expectation that v_3 is mostly or entirely driven by ε_3, and v_5 by ε_5. We will revisit this below. $\psi_2^{\rm PP}$ and $\psi_2^{\rm EP}$ are strongly correlated with the reaction plane, at least for this mixed-centrality set of events. This is expected since, for non-central collisions, ε_2 is mostly controlled by the almond-shaped overlap geometry, and v_2

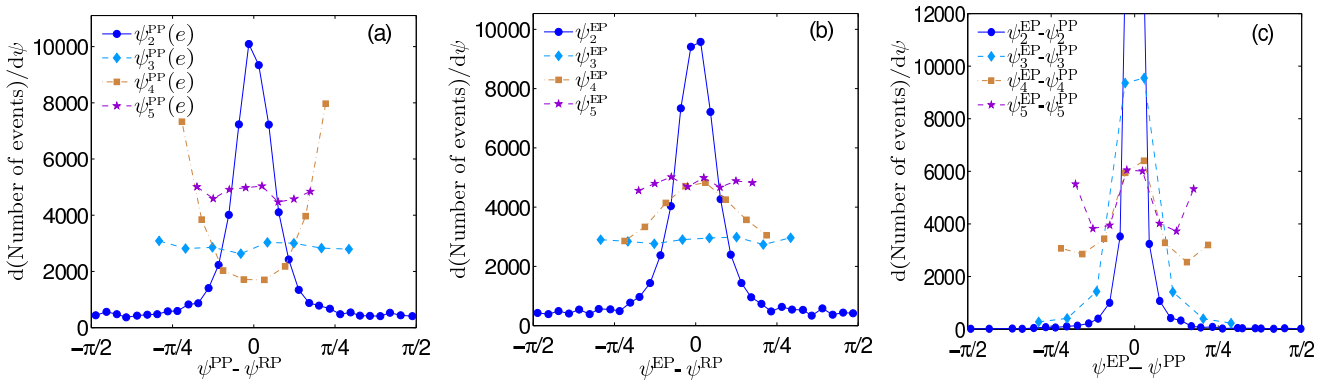


FIG. 7: (Color online) Event-by-event correlation of the participant plane (PP,(a)) and event plane (EP,(b)) angles with the reaction plane (RP), as well as the correlation between participant and event plane angles (c), for different harmonic eccentricity and flow coefficients. The same 6000 events as in Fig. 4 were analyzed.

is mostly a collective flow response to this geometric deformation; event-by-event fluctuations contribute to ε_2 (and thus v_2), but in general do not dominate them.

The behavior of $\psi_4^{\rm PP}$ in Fig. 7a is interesting because it is on average strongly "anti-correlated" with the reaction plane, in the sense that it points (on average) at 45° relative to the x-axis. The geometric reason for this has already been discussed above in subsection III D. On the other hand, Fig. 7b shows that the angle $\psi_4^{\rm EP}$ points on average *into* the reaction plane. This correlation of $\psi_4^{\rm EP}$ with the reaction plane is somewhat weaker than the anti-correlation of $\psi_4^{\rm PP}$ with that plane seen in panel (a). Still, it suggests that quadrangular flow v_4 does not, on average, develop predominantly in the direction of the steepest pressure gradient associated with ε_4, but in the direction of steepest ε_2-induced pressure gradient. This can be understood as follows: since ε_2 generates a second harmonic deformation of the flow velocity profile which elliptically deforms *the exponent* of the flow-boosted Boltzmann factor $\exp[-p\cdot u(x)/T(x)]$ describing the local thermal momentum distribution of particles, it leads to harmonic contributions v_{2k} of *all* even orders $n=2k$ in the momentum distributions of the finally emitted particles [50]. Fig. 7b suggests that, on average, this effect wins over initial-state quadrangular deformation effects.

Figure 7c, however, in which we analyze directly the correlation between the event and participant plane angles, paints a more subtle picture. It shows, surprisingly, a correlation peak at zero relative angle between $\psi_4^{\rm EP}$ and $\psi_4^{\rm PP}$, whereas the above discussion should have led us to expect a correlation peak at 45°. The resolution of this paradox is presented in the next subsection: The relative importance of geometric and fluctuation-induced contributions to ε_n, v_n, and their associated angles changes with collision centrality, with geometry playing a relatively larger role in peripheral collisions. One should therefore look at the angle correlations as a function of collision centrality. One finds that the correlation function peaks in Figs. 7a,b for the $4^{\rm th}$-order angles relative to the reaction plane are almost entirely due to geometric effects in peripheral collisions, while in central collisions both $\psi_4^{\rm PP}$ and $\psi_4^{\rm EP}$ are fluctuation-dominated and thus essentially uncorrelated with the reaction plane. On the other hand, precisely because in central collisions geometric effects such as geometrically driven elliptic flow do not dominate the hydrodynamic response to the fluctuation-driven higher-order eccentricities, $\psi_4^{\rm EP}$ and $\psi_4^{\rm PP}$ remain relatively strongly correlated in near-central collisions. This is the reason for the peak at 0° for $n=4$ in Fig. 7c. (A hint of the "anti-correlation" at 45° is still visible in Fig. 7c, and it would be stronger if we had not (for unrelated reasons) strongly oversampled central collisions in our mixed-centrality sample.)

We close this discussion with the following additional observations about Fig. 7c: (i) The second-order participant and event planes are much more strongly correlated with each other than either one of them is with the reaction plane. This shows that even in very central collisions, where the source ellipticity is mostly fluctuation-driven and its angle therefore only weakly correlated with the reaction plane, elliptic flow develops event-by-event in the direction of the short axis of the ellipsoid. (ii) Even though the angles associated with ε_3 and v_3 are uncorrelated with the reaction plane (Figs. 7a,b), they are strongly correlated with each other. This indicates that v_3 is mostly driven by ε_3, especially in the more central collisions, with relatively little interference from other harmonics. (iii) The $5^{\rm th}$-order event and participant plane angles show correlation peaks both at 0 and $\pi/5$. As we will see in the following subsection, the former results from central and the latter from peripheral collisions. The peak at $\pi/5$ indicates significant cross-feeding between modes with $n=2$, 3, and 5.

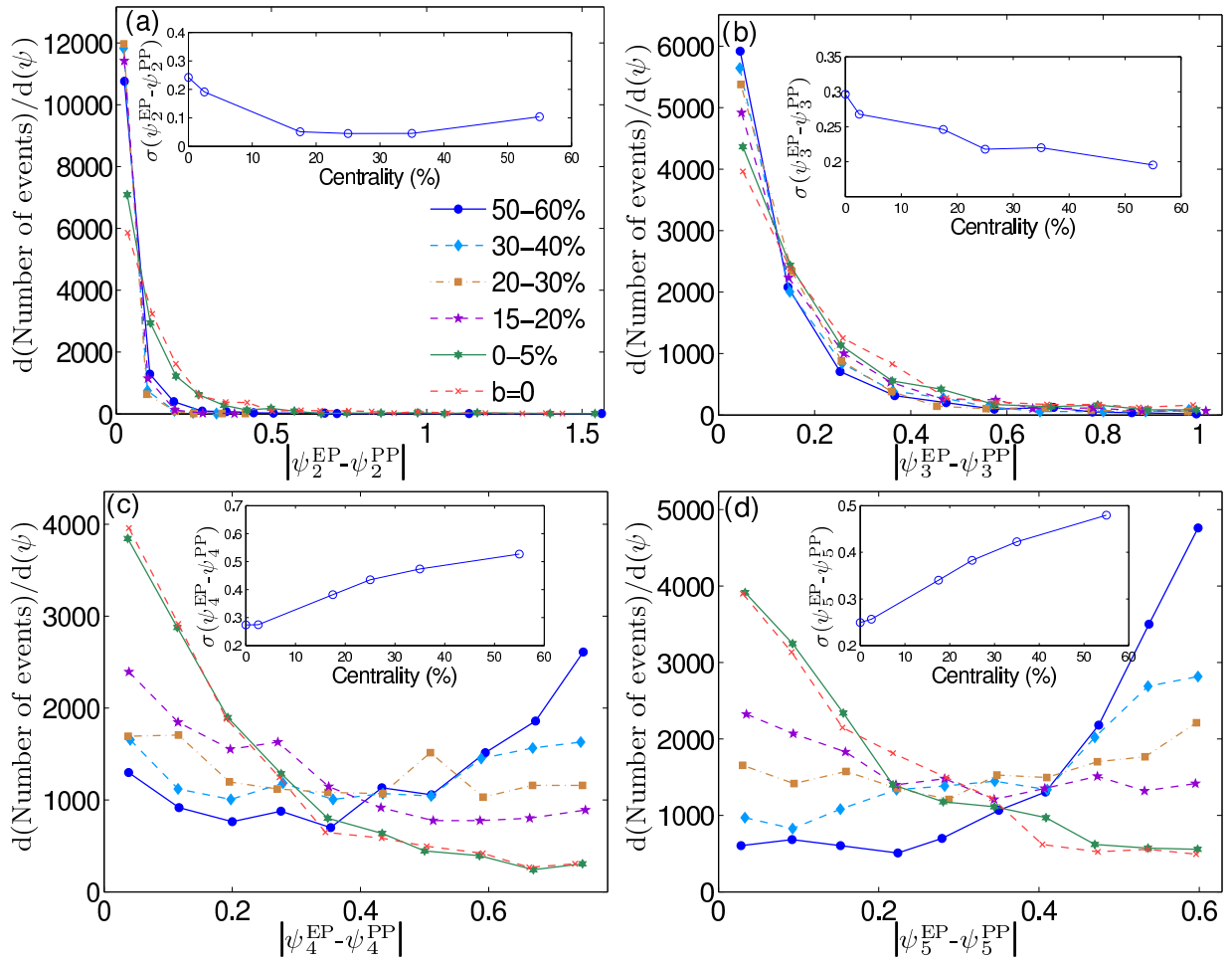


FIG. 8: (color online) Event-by-event correlation between the absolute values of the event plane (EP) and participant plane (PP) angles for the harmonics of order $2-5$ (panels (a)-(d)), for events in different centrality classes as indicated in the legend. (The same set of MC-KLN events as in Fig. 4 was used.) The insets show the centrality dependence of the widths of these correlations around zero.

B. Centrality dependence of event and participant plane correlations

Figure 8 looks at the correlation between the n^{th}-order EP and PP angles at different collision centralities. This generalizes a similar analysis for $n=2$ in Ref. [29] to higher harmonics. Plotted are the distributions of the absolute value of the difference between the two angles in the main graph and the rms of this distribution (i.e. the width around zero of the correlation) in the inset, as a function of collision centrality. Panel (a) shows that the second-order participant and event planes are strongly correlated at all collision centralities. This demonstrates that elliptic flow is generated almost exclusively by the source ellipticity. The variance of the correlation is ~ 0.05 rad in the mid-central range (15-40% centrality) and increases in very central and very peripheral collisions due to growing ellipticity fluctuations.

A similar correlation exists for the 3^{rd}-order participant and event planes, at all collision centralities, but with a larger variance of order $0.2-0.3$ rad (depending on centrality). The relatively strong correlation suggests that ε_3 is the dominant driver for v_3 [19].

For the 4^{th}- and 5^{th}-order participant and event planes the situation is complicated, as seen in panels (c) and (d). The planes are correlated with each other (i.e. the distributions peak at zero difference angle) in central collisions, become essentially uncorrelated in mid-central collisions and anti-correlated (i.e. peaked at a difference angle of π/n, $n=4,5$) in peripheral collisions. The anti-correlation in peripheral collisions indicates strong mode-mixing, driven by the large ellipticity ε_2 and strong elliptic flow v_2 at large impact parameters which generates v_4 and v_5 contributions by coupling to lower harmonics, as described in the previous subsection. For v_4 in particular, a strong $\cos(2\phi)$ component in the collective flow velocity generates a v_4 of the final momentum distribution, without any need for nonzero ε_4. At large impact

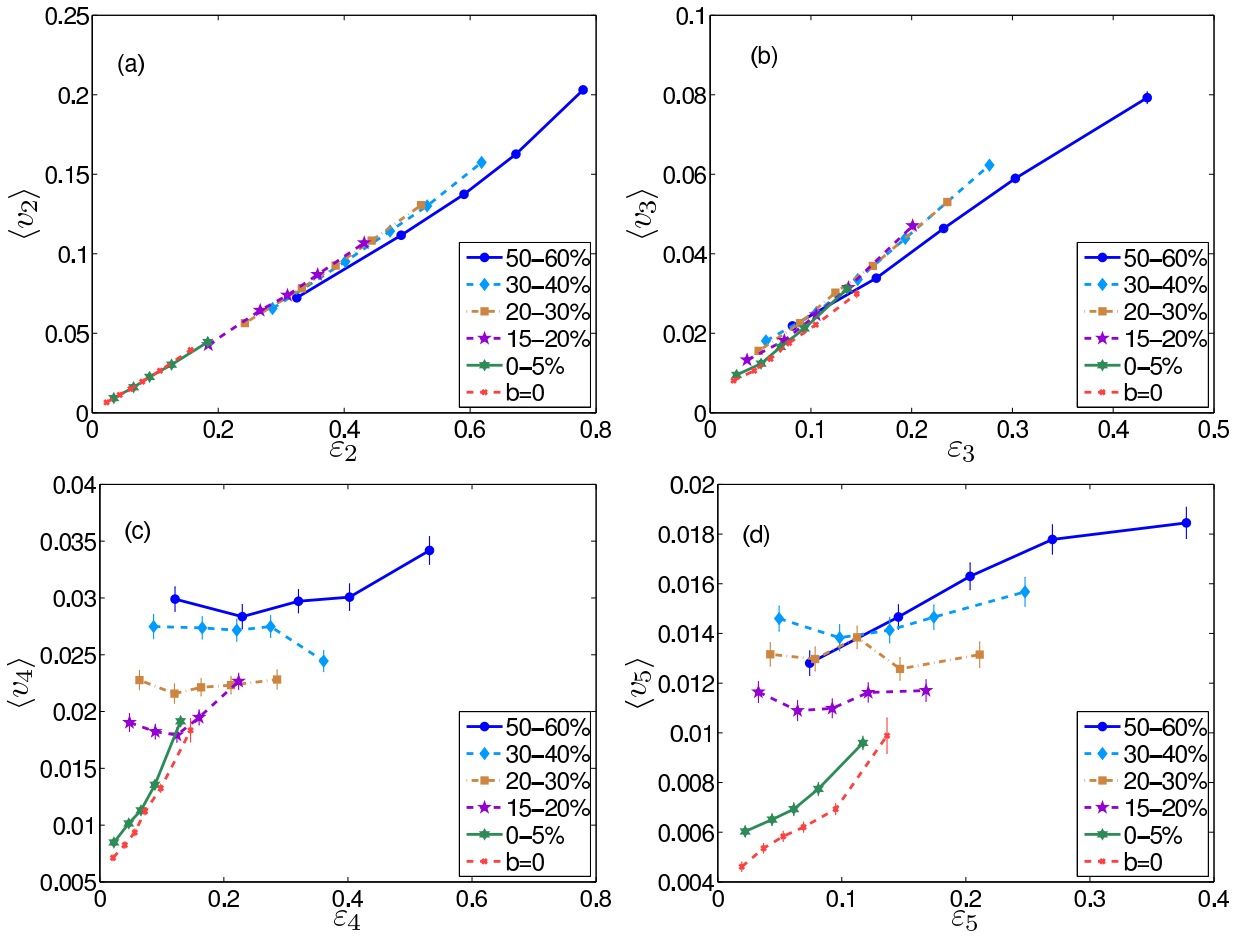


FIG. 9: (Color online) $\langle v_n \rangle(\varepsilon_n)$ for $n = 2, 3, 4, 5$ (panels (a)-(d)). As in Fig. 4, each centrality class contains 1000 MC-KLN events, grouped in eccentricity bins of sufficient width to have reasonable statistics in each bin.

parameters, ε_2-induced quadrupolar flow from the initial elliptic deformation of the overlap region thus dominates over any contribution from initial quadrangular deformation. In near-central collisions, on the other hand, where all ε_n stem mostly from shape fluctuations, $v_{4,5}$ are dominantly driven by $\varepsilon_{4,5}$.

C. Harmonic flows and their corresponding initial eccentricities: nonlinear hydrodynamic response

As discussed in the Introduction, it is often assumed that the harmonic flows v_n respond linearly to the eccentricities ε_n, at least as long as the latter are small. This assumption receives support from hydrodynamic simulations [26] as long as one probes deformed initial profiles with only a single non-vanishing harmonic eccentricity coefficient. In Fig. 9 we investigate the validity of this assumption with fluctuating MC-KLN events which feature nonzero ε_n values for all n.

Figure 9a generally provides support for the assumption of a linear dependence of the elliptic flow v_2 on initial ellipticity ε_2, with two important caveats:

(i) At small and large ellipticities, v_2 deviates upward from a best-fit line through the origin, indicating additional contributors to the elliptic flow. Indeed, for zero ellipticity $\varepsilon_2 = 0$ we find a nonzero average $\langle v_2 \rangle$. These are events with typically large nonzero values for eccentricities of higher harmonic order which generate elliptic flow through mode-mixing (e.g. between ε_3 and ε_5). We see that this happens at all centralities, even for $b = 0$, due to event-by-event fluctuations of the eccentricity coefficients.

(ii) The slope of the curve $\langle v_2 \rangle(\varepsilon_2)$ decreases in very peripheral collisions, indicating destructive interference via mode-mixing from other harmonics in the hydrodynamic evolution of the small and highly fluctuating fireballs created at large impact parameters.

The ε_3-dependence of triangular flow $\langle v_3 \rangle$, shown in Fig. 9b, shows a qualitatively similar story, but the deviations from linear response are stronger, with significant non-zero triangular flow in events with zero initial triangularity, especially for larger impact parameters.

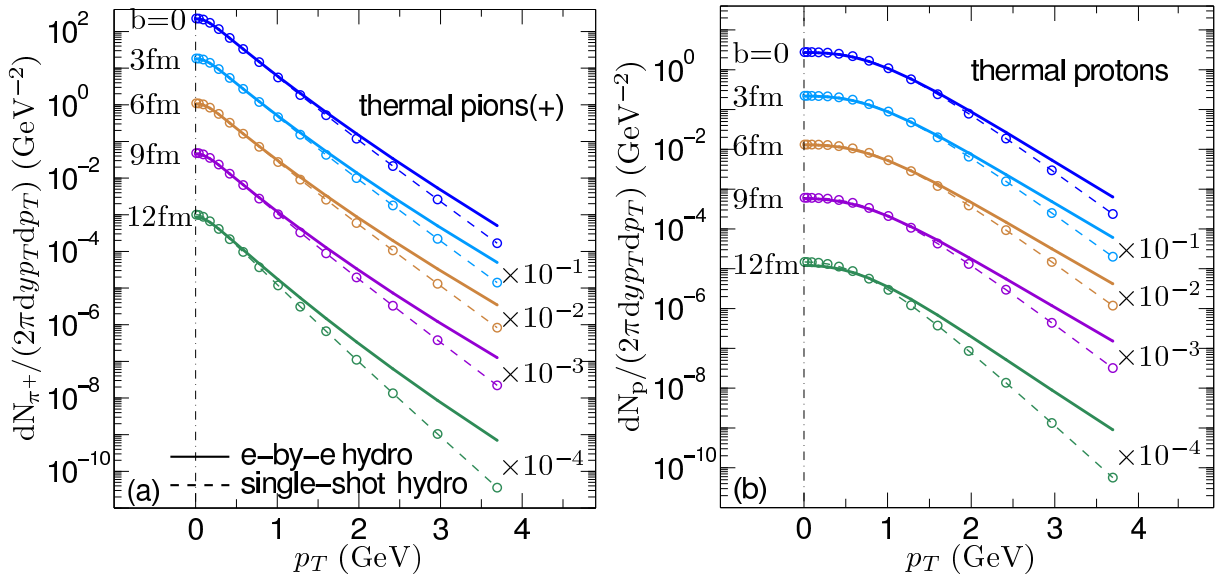


FIG. 10: (Color online) Transverse momenrum spectra for directly emitted π^+ (a) and protons (b) from event-by-event (solid lines) and single-shot hydrodynamics (dashed lines), for 200 A GeV Au+Au collisions at five selected impact parameters.

For $\langle v_4 \rangle$ and $\langle v_5 \rangle$, shown in Figs. 9c and 9d, mode-mixing effects are very strong, and a linear response of v_n to ε_n ($n = 4, 5$) can no longer be claimed. This is quite different from the results in [26] where v_4 was studied for a source that had only ε_4 deformation: in this case $v_4(\varepsilon_4)$ was found to be approximately linear for small ε_4, with a downward bend at larger ε_4 values due to negative interference from cross-currents for sources with large quadrangularities. (This approximately linear dependence survived in the p_T-integrated v_4 even though it was noticed in a related study [51] that, for mid-central collisions, the differential quadrangular flow $v_4(p_T)$ appears at high p_T to be mostly determined by the elliptic deformation of the hydrodynamic flow profile generated by ε_2.) Our present study shows that it is unlikely that the anisotropic flow resulting from highly inhomogeneous initial profiles with nonzero eccentricity coefficients of all harmonic orders can be obtained by some sort of linear superposition of flows generated from sources with only a single nonzero harmonic eccentricity coefficient, as suggested [38]. The hydrodynamic response $\{v_n\}$ to a set of initial eccentricity coefficients $\{\varepsilon_n\}$ is not only non-diagonal, but also (via mode-mixing) non-linear, and there is no suitable single-shot substitute for event-by-event hydrodynamic evolution of fluctuating initial conditions.

We note, however, that non-linear mode-mixing effects appear to be minimal for the elliptic and triangular flow (Figs. 9a,b). v_2 and v_3 remain therefore the best candidates for an extraction of the fluid's viscosity, by studying (with quantitative precision) the fluid's efficiency in converting initial spatial deformations into final momentum anisotropies and anisotropic flows. We will further elaborate on this theme in the next section.

V. SINGLE-SHOT VERSUS EVENT-BY-EVENT HYDRODYNAMICS

We now discuss the effects of event-by-event initial-state fluctuations on the finally observed pion and proton p_T-spectra and anisotropic flow, comparing traditional single-shot hydrodynamic evolution of an appropriately constructed smooth average initial profile with event-by-event evolution of fluctuating initial conditions (with an ensemble average taken at the end). Since the calculation of resonance decay feeddown corrections is computationally expensive but not expected to cause qualitative changes, we here concentrate on directly emitted ("thermal") pions and protons. For the graphs shown in this section, we generated for each impact parameter 1000 fluctuating events and propagated them either individually ("event-by-event hydrodynamics") or in a single hydrodynamic run after rotating and averaging their profiles ("single-shot hydrodynamics") down to a decoupling temperature of 120 MeV.

A. Transverse momentum spectra

In a very interesting recent paper [31] Chatterjee *et al.* showed that thermal photon spectra from exploding heavy-ion collision fireballs with fluctuating initial conditions which were hydrodynamically evolved event-by-event are significantly harder than those obtained from single-shot hydrodynamic evolution of the corresponding

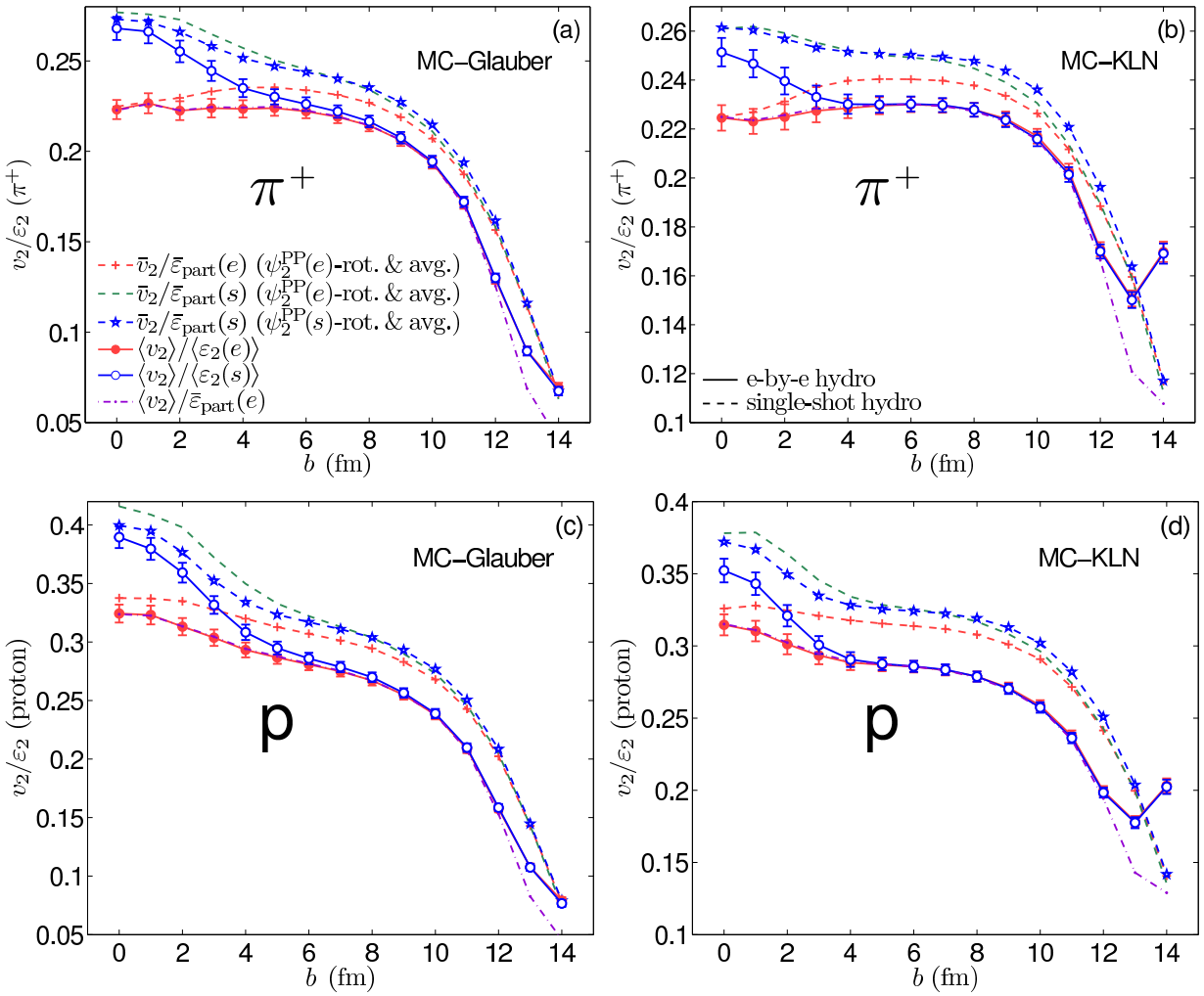


FIG. 11: (Color online) Eccentricity-scaled elliptic flow v_2/ε_2 as function of impact parameter, for pions (panels (a,b)) and protons (panels (c,d)), from the ideal fluid dynamic evolution of initial MC-Glauber (a,c) and MC-KLN (b,d) density profiles. Solid (dashed) lines correspond to event-by-event (single-shot) hydrodynamics. See text for discussion.

ensemble-averaged (and therefore much smoother) initial profiles. The authors of [31] attributed this effect to the existence of "hot spots" in the fluctuating initial conditions that radiate photons at a higher than average temperature. Figure 10 shows that the same hardening occurs in the pion and proton spectra even though these strongly interacting hadrons are emitted only at freeze-out, with the same decoupling temperature assumed in both types of evolution.[5] This proves that the effect is due to stronger radial flow in the event-by-event evolved fluctuating fireballs, driven by the stronger than average pressure gradients associated with the "hot spots" (i.e. over-dense regions) in the initial profile. The importance of initial-state fluctuation effects on the final p_T-spectra becomes stronger in peripheral collisions where the initial fireballs are smaller and "hot spots" have a relatively larger influence. If stronger radial flow is the explanation of the fluctuation-driven hardening of the pion and proton spectra observed in Fig. 10, it is probably also a dominant contributor to the hardening of the photon spectra noted in Ref. [31], at least for low p_T (i.e. in the hydrodynamic regime). This could be checked by comparing the photon radiation from the late hadronic stage in event-by-event and single-shot hydrodynamics which, if our interpretation is correct, should show the same fluctuation-driven, flow-induced hardening as the total photon spectra.

[5] A similar effect was also seen in [29] whose authors further pointed out that the strength of this "hardening effect" depends on the fluctuation size parameter in the initial conditions (i.e. the area over which the entropy produced in a nucleon-nucleon collision is distributed).

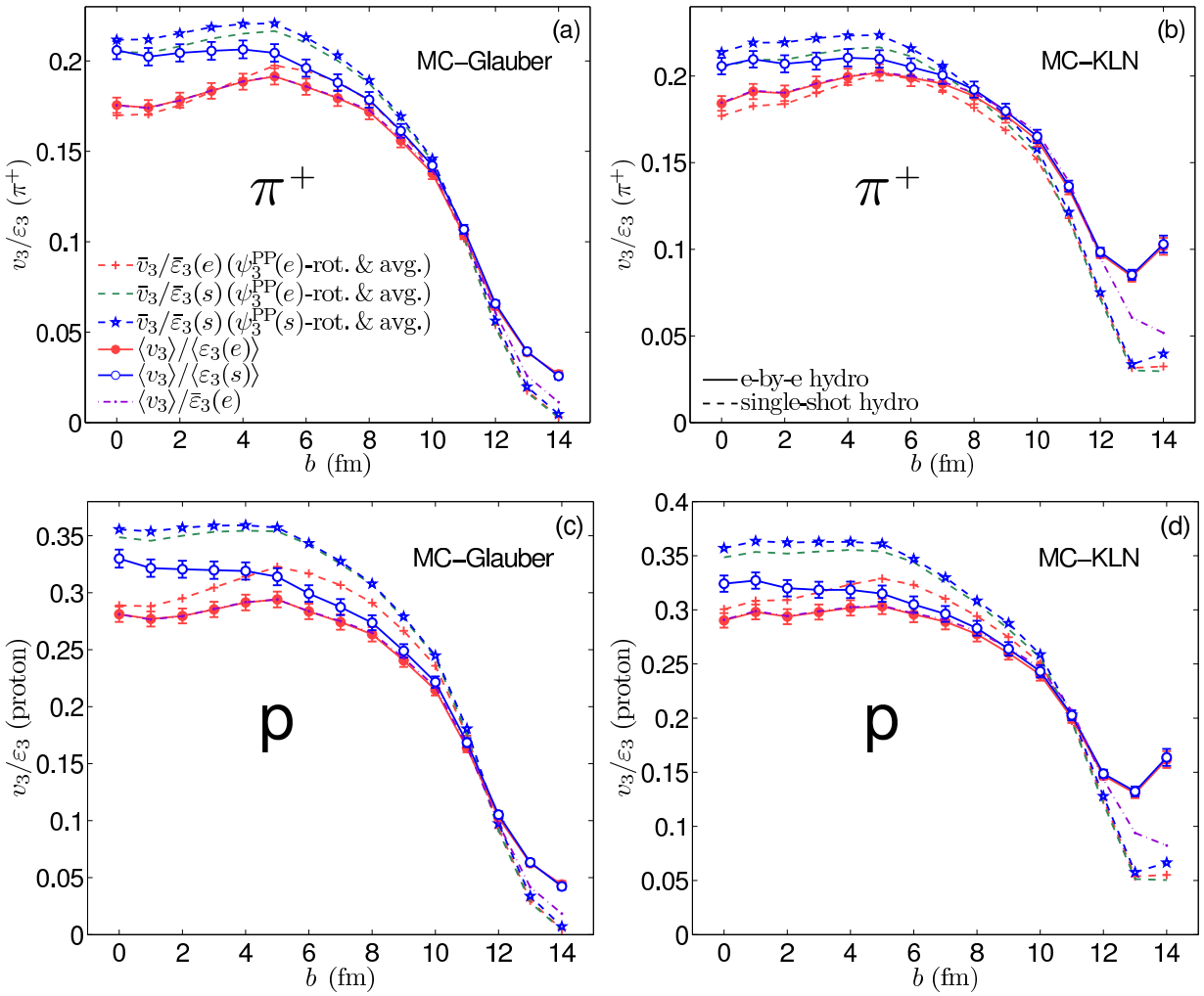


FIG. 12: (Color online) Same as Fig. 11, but for the eccentricity-scaled triangular flow v_3/ε_3.

B. Elliptic and triangular flow

In Figures 11 and 12, we compare the eccentricity-scaled elliptic and triangular flows, v_2/ε_2 and v_3/ε_3, for pions and protons as a function of impact parameter, from single-shot (dashed lines) and event-by-event hydrodynamics (solid lines). These ratios represent the efficiency of the fluid for converting initial spatial deformations into final-state momentum anisotropies. This conversion efficiency is affected (i.e. reduced) by shear viscosity, so these ratios form the basis of many analyses that aim to extract this transport coefficient from experimental heavy-ion data.

For event-by-event hydrodynamics we show two curves, using either the entropy density (blue open circles) or the energy density weighted (red solid circles) average eccentricities to normalize the average final flow $\langle v_n\rangle$. For the ellipticity (Fig. 11) this choice is seen to make a difference only in rather central collisions ($b<4$ fm), but for the triangularity the differences are significant out to average impact parameters probed in minimum bias samples, $b\lesssim 8$ fm. As stated earlier, we prefer the energy density weighted eccentricities (solid circles) as deformation measures because energy density and pressure are closely related through the EOS, and it is the pressure gradients (and their anisotropies) that drive the collective flow (and its anisotropies).

For the single-shot hydrodynamic simulations, a question arises as to how exactly one should construct the ensemble-averaged smooth initial profile which is then evolved hydrodynamically. We have explored three reasonable procedures (variations of which have been used in the literature) and show them as dashed lines in Figs. 11 and 12. For the *lines labeled by stars*, we rotate the entropy density for each fluctuating event by the corresponding entropy-weighted participant-plane angle $\psi_n^{\rm PP}(s)$ ($n=2,3$, see Eq. (19)),[6] then average the rotated

[6] Note that for computation of $\bar{v}_3$ we rotate the events by a differ-

entropy profiles, compute the eccentricity $\bar{\varepsilon}_n(s)$ of the resulting average entropy density profile and convert it to energy density using the EOS for input into the hydrodynamic code. For the *lines labeled by crosses*, we rotate the energy density for each fluctuating event (obtained from the EOS) by the corresponding energy-weighted participant-plane angle $\psi_n^{\rm PP}(e)$ (see Eqs. (1,2)), compute the averaged rotated energy density profile and its eccentricity $\bar{\varepsilon}_n(e)$, and use it directly as hydrodynamic input. For the *dashed lines without symbols*, finally, the averaged initial energy density (and therefore the final $\bar{v}_n$) are exactly the same as for the lines with crosses, but the final $\bar{v}_n$ is scaled by the entropy-weighted (rather than energy-weighted) eccentricity of the averaged initial profile, where the entropy density is obtained from the smooth averaged energy density via the EOS.

The differences between the different dashed lines illustrate the uncertainties associated with the choice of averaging procedure for the initial state. Keeping in mind that a 20% reduction in v_2/ε_2 corresponds (very roughly) to an increase of η/s by $1/4\pi$ [5], one sees that these differences are not negligible if one aims for quantitative precision in the extraction of the specific shear viscosity. Comparing the three dashed lines we see that it doesn't make much difference whether we use the s-weighted or e-weighted participant-plane angles to rotate the events before superimposing them (the dashed lines without symbols and with stars are all very close to each other), but that in the more central collisions we obtain significantly different values for the conversion efficiencies $\bar{v}_n/\bar{\varepsilon}_n$ if we normalize by e- or s-weighted mean eccentricities. Even though they look similar in Fig. 5a, at small impact parameters $\bar{\varepsilon}_{\rm part}(e)$ and $\langle\varepsilon_2(e)\rangle$ are larger than $\bar{\varepsilon}_{\rm part}(s)$ and $\langle\varepsilon_2(s)\rangle$, respectively, and this is the main reason why the red and blue lines in Fig. 11 diverge at small b, for both event-by-event (solid lines) and single-shot hydrodynamics (dashed lines).

An apples-to-apples comparison between event-by-event and single-shot hydrodynamics (and between theory and experimental data) therefore must ensure that the same (or at least conceptually compatible) eccentricities are used to normalize the anisotropic flow coefficients that are to be compared. In Figs. 11, 12 we should therefore compare blue solid with blue dashed, or red solid with red dashed lines, but not curves of different colors.

Even this is not good enough if one wants to accurately assess the relative space-to-momentum anisotropy conversion efficiency in single-shot and event-by-event hydrodynamics: in the single-shot hydro curves we use $\bar{\varepsilon}_{\rm part}$ to normalize the final elliptic flow, whereas the event-by-event hydro results were normalized with $\langle\varepsilon_2\rangle \equiv \langle\varepsilon_{\rm part}\rangle$. While each of these eccentricity measures makes perfect sense in its own context, they differ at large impact parameters, $\bar{\varepsilon}_{\rm part}$ being larger (see Figs. 1a,b). To avoid this problem we have added in Figs. 11 and 12 an additional "mixed ratio" (dash-dotted purple line) which normalizes the ensemble-averaged anisotropic flow $\langle v_n\rangle$ ($n=2,3$) from event-by-event hydrodynamics (used in the ratio $\langle v_n\rangle/\langle\varepsilon_n\rangle$ denoted by solid lines with solid red circles) by the mean e-weighted eccentricity $\bar{\varepsilon}_n$ from single-shot hydrodynamics (used in the ratio $\bar{v}_n/\bar{\varepsilon}_n$ denoted by dashed lines with crosses). This dot-dashed purple line agrees almost perfectly with the solid red line with circles over most of the impact parameter range, except for peripheral collisions with $b \gtrsim 10$ fm where $\bar{\varepsilon}_n$ and $\langle\varepsilon_n\rangle$ begin to diverge. The red dashed lines with crosses and purple dash-dotted lines show the anisotropic flows from single-shot and event-by-event hydrodynamics normalized by the *same* eccentricity measure characterizing the fluctuating event sample. Their comparison allows an unambiguous assessment of the different efficiencies of single-shot and event-by-event hydrodynamics in converting initial eccentricities to final momentum anisotropies. Their ratio is shown in Fig. 13.

From Fig. 13a one concludes that, for ideal hydrodynamics, event-by-event fluctuations on average reduce the efficiency of the fluid in converting initial source ellipticity into elliptic flow. Over most of the centrality range this reduction is about 4% for pions and about twice as large for protons, and it is similar for MC-KLN and MC-Glauber initial profiles. In very central collisions the ratio of conversion efficiencies for event-by-event vs. single-shot hydrodynamics is closer to 1, but it degrades strongly in very peripheral collisions where event-by-event evolution generates on average 30−40% less elliptic flow than single-shot hydrodynamics. The generic tendency of event-by-event hydrodynamic evolution of fluctuating initial profiles to generate less elliptic flow than expected from hydrodynamic evolution of the corresponding smooth average profile has been observed before [27, 30]; our systematic study in Fig. 13a quantifies this effect over the full range of collision centralities.

The situation with triangular flow, shown in Fig. 13b, is quite different: event-by-event propagation of initial-state flutuations can lead to an increase or decrease of the triangular flow compared to single-shot hydrodynamics, depending on particle mass (pions or protons), the nature of the fluctuations (MC-Glauber or MC-KLN), and collision centrality. Contrary to elliptic flow, in peripheral collisions event-by-event evolution leads to significantly *larger* average triangular flow than single-shot hydrodynamics.

We expect that non-zero viscosity will dampen fluctuation effects and somewhat reduce the differences between event-by-event and single-shot hydrodynamic evolution of elliptic and triangular flow shown in Fig. 13. Nevertheless it appears that, for quantitative studies of the influence of viscosity on the generation of anisotropic collective flow, event-by-event hydrodynamic evolution is an essential and indispensable ingredient.

---

ent angle before averaging than for $\bar{v}_2$, i.e. $\bar{v}_3$ and $\bar{v}_2$ are obtained from two different single-shot hydrodynamic runs, starting from different averaged initial energy density profiles.

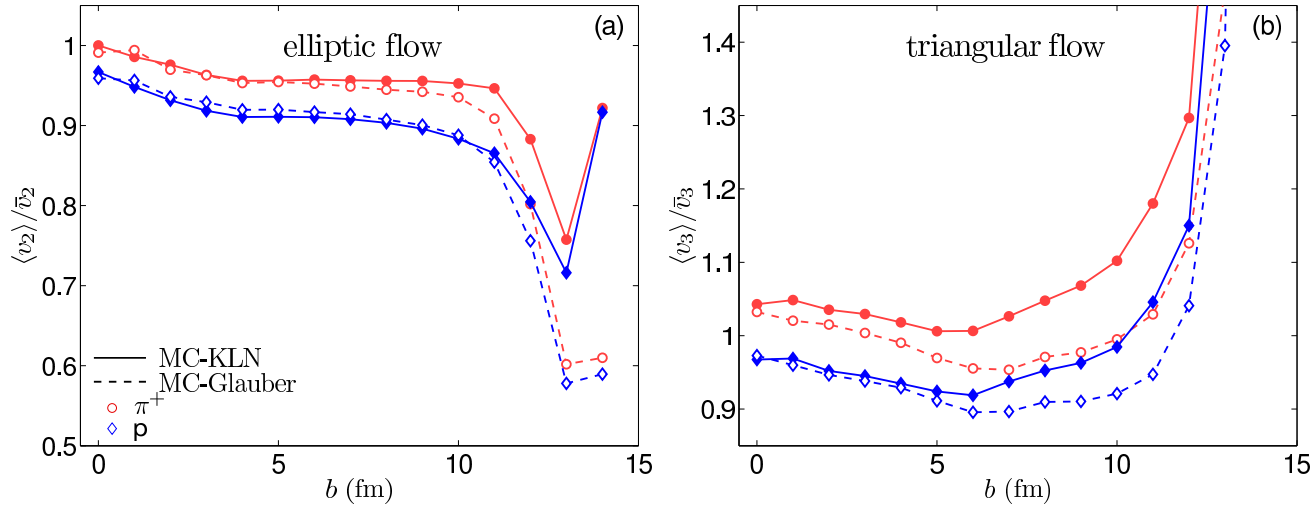


FIG. 13: (Color online) Ratio of the average flow coefficient $\langle v_n\rangle$ from event-by-event hydrodynamics and the corresponding mean $\bar{v}_n$ from single-shot hydrodynamics, as a function of impact parameter in 200 A GeV Au+Au collisions, for $n=2$ (a) and $n=3$ (b). Shown are the ratios for directly emitted pions (circles) and protons (diamonds) from fluctuating events using the MC-Glauber (dashed lines) and MC-KLN models (solid lines). Average events for computing $\bar{v}_n$ using single-shot hydrodyamics were obtained by rotating the energy density of each event by $\psi_n^{\rm PP}(e)$ before superimposing them.

C. Elliptic flow fluctuations

Similar to what is shown in Figs. 1a,b for the initial source ellipticities, Fig. 14 shows the elliptic flow measures $\langle v_2\rangle$, $v_2\{2\}$ and $v_2\{4\}$ from event-by-event hydrodynamics, together with $\bar{v}_2$ from single-shot hydrodynamic evolution of the corresponding averaged initial profile, for pions and protons, using MC-Glauber and MC-KLN initializations, respectively. $v_2\{2\}$ and $v_2\{4\}$ are defined in analogy to Eqs. (9,10) by

$$v_2\{2\}^2 = \langle v_2^2\rangle, \tag{23}$$
$$v_2\{4\}^4 = 2\langle v_2^2\rangle^2 - \langle v_2^4\rangle. \tag{24}$$

Here v_2 is calculated event-by-event via Eq. (22) from the Cooper-Frye spectrum at freeze-out (with zero statistical uncertainties since it is determined with mathematical precision by the event-by-event hydrodynamic output).

As in Fig. 1, open stars show the central values for $\sqrt[4]{|v_2\{4\}^4|}$ whenever $v_2\{4\}^4$ turns negative, and open-ended error bars indicate that the error band for $v_2\{4\}^4$ ranges from positive to negative values. Similar to the ellipticities shown in Fig. 1, the latter happens at small impact parameters, but for the MC-Glauber model the b-range over which this happens for $v_2\{4\}$ (for both pions and protons) is somewhat larger than for $\varepsilon\{4\}$. Still, $v_2\{4\}$ is compatible with zero over this entire range, and we do not find statistically significant negative values for $v_2\{4\}$ at small impact parameters. At large $b>12$ fm $v_2\{4\}^4$ turns negative for both pions and protons when we use MC-Glauber initial conditions whereas it remains positive for MC-KLN initial profiles.

By comparing $\bar{v}_2$ (open circles in Fig. 14) with $\langle v_2\rangle$ (solid green circles) one sees that in mid-central to peripheral collisions the v_2-suppression from event-by-event hydrodynamic evolution is of the same order as or (especially for protons) even larger than the difference between $v_2\{2\}$ and $\langle v_2\rangle$ (solid blue vs. solid green circles) that arises from event-by-event flow fluctuations. As a result, $v_2\{2\}$ from event-by-event hydrodynamics lies in peripheral collisions even below $\bar{v}_2$ from single-shot hydrodynamics, in spite of its fluctuation-induced enhancement.

Similar to Eqs. (11)-(13) we can test whether the v_2 fluctuations from event to event have Gaussian or Bessel-Gaussian distributions. This is done in Fig. 15. The upper set of curves (thick lines) test the v_2-analogue of relation (13) whereas the lower set (thin lines) tests the validity of Eq. (11). (In the lower set of curves we dropped all b-values for which the error band for $v_2\{4\}^4$ extends ton negative values.) Just as we saw for the initial ellipticities in Fig. 3, both the Gaussian and Bessel-Gaussian hypotheses for v_2-fluctuations are seen to hold quite well in mid-central ($4\lesssim b\lesssim 10$ fm) collisions. The Bessel-Gaussian hypothesis breaks down in peripheral collisions ($b>10$ fm). Whether it holds (as expected [22]) in central collisions is a question that, with our present statistics of 1000 events per b-value, we can not reliably answer, but we see no indications for the opposite. The assumption of Gaussian v_2-fluctuations breaks down in central collisions ($b<5$ fm), as expected. For the MC-Glauber model it also breaks down in very peripheral collisions, whereas for MC-KLN initial conditions the final elliptic flow exhibits a nice Gaussian distribution all the way to the largest impact parameters.

Overall, a comparison of Figs. 15 and 3 (as well as of Figs. 14 and 1) shows that the statistical properties of v_2 fluctuations are qualitatively similar but quantitatively different from those of the initial ellipticity fluctuations.

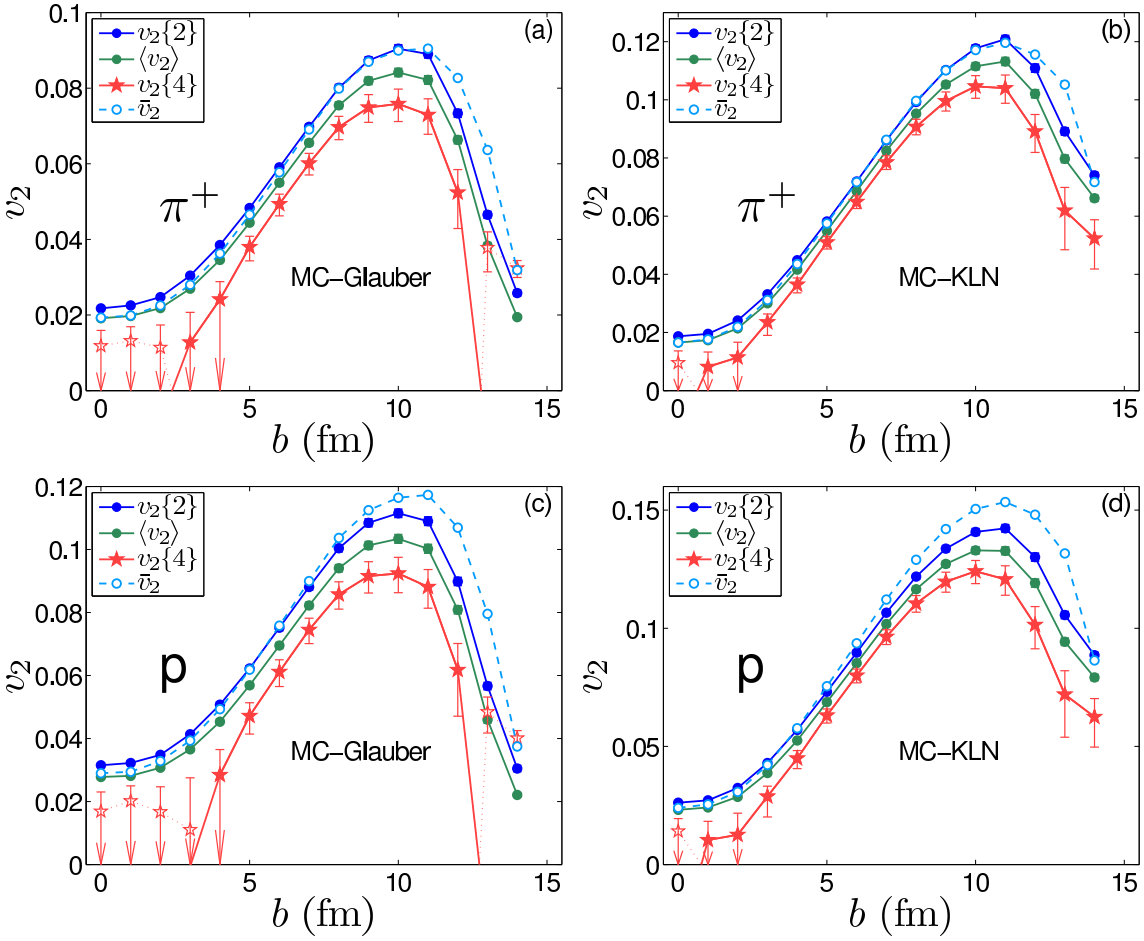


FIG. 14: (Color online) Different measures for the final elliptic flow v_2 (similar to Fig. 1) for directly emitted pions (a,b) and protons (c,d) as functions of impact parameter from event-by-event ideal fluid dynamics, using MC-Glauber (a,c) and MC-KLN (b,d) initial conditions for 200 A GeV Au+Au collisions.

This is consistent with the fact that the main driver for elliptic flow is the initial ellipticity, but that eccentricity coefficients of higher harmonic orders affect the evolution of v_2 weakly but measurably through non-linear mode-coupling effects.

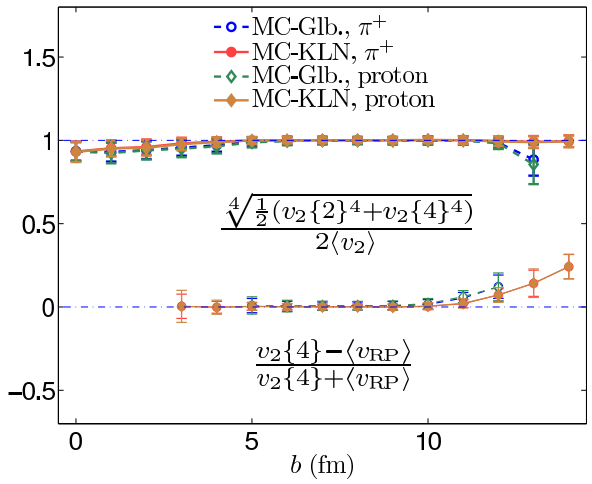


FIG. 15: (Color online) Similar to Fig. 3, but for the elliptic flow v_2 of pions and protons. See text for discussion.

VI. SUMMARY AND CONCLUSIONS

In this work we presented a comprehensive analysis of event-by-event shape fluctuations in the initial state and flow fluctuations in the final state of relativistic heavy-ion collisions, as quantified by the first four non-trivial harmonic eccentricity and flow coefficients, ε_n and v_n $(n=2,3,4,5)$. Using the MC-Glauber and MC-KLN models to generate fluctuating initial entropy and energy density profiles, we explored the centrality dependence of a number of different variants of these anisotropy measures that are being used by practitioners in the field, and compared them with each other. Although they all exhibit similar qualitative behaviour, quantitative differences exist and must be carefully taken into account in the theoretical analysis of experimental data. As far as we know, ours is the first comprehensive analysis quan-

tifying these differences for both the Glauber and Color Glass Condensate models.

We list a few key results:
– The average and mean ellipticities $\langle\varepsilon_2\rangle$ and $\bar{\varepsilon}_2$ agree with excellent accuracy over a wide range of impact parameters, but diverge in very peripheral collisions ($\geq 60\%$ centrality) where $\bar{\varepsilon}_2 > \langle\varepsilon_2\rangle$ (both for participant-plane and reaction-plane averaged profiles).
– The average energy and entropy density weighted eccentricities agree with excellent accuracy over a wide range of impact parameters, except for central collisions ($b \lesssim 4\,\mathrm{fm}$) where $\langle\varepsilon_n(e)\rangle > \langle\varepsilon_n(s)\rangle$.
– Whether the fluctuating entropy density distributions for individual events are first converted to energy density and then rotated by $\psi_n^{\mathrm{PP}}(e)$ and averaged, or first rotated by $\psi_n^{\mathrm{PP}}(s)$ and averaged and then converted to energy density has very little influence on the shape of the resulting smooth average initial energy density profile for single-shot hydrodynamics. We prefer (and propose as standard procedure) the conversion to energy density as the first step, since in event-by-event hydrodynamics the energy density gradients of each event generate (through the EOS) the pressure gradients that drive the evolution of collective flow.
– The shortcut of using reaction-plane averaging to generate a smooth profile for single-shot hydrodynamics with ellipticity approximately equal to $\varepsilon\{4\}$ of the ensemble, in the hope of generating with a single hydrodynamic run an elliptic flow $\bar{v}_2$ that can be directly compared with $v_2\{4\}$ measurements, works only in the 0−40% centrality range. For peripheral collisions this method cannot be trusted.
– The assumption of Bessel-Gaussian fluctuations for initial source ellipticity and final elliptic flow work well for $b \lesssim 10\,\mathrm{fm}$ but breaks down in more peripheral collisions. For more peripheral collisions the hypothesis that ε_2 and v_2 are Gaussian distributed works better than the Bessel-Gaussian assumption, but it breaks down for $b < 5\,\mathrm{fm}$. For MC-Glauber initial conditions, directly emitted pions and protons feature negative values of $v_2\{4\}^4$ in very peripheral collisions. The fluctuations of initial source ellipticities and final elliptic flow values have qualitatively similar but quantitatively different statistical properties.
– Except for rather central collisions, the eccentricities $\langle\varepsilon_2\rangle$, $\langle\varepsilon_4\rangle$ and $\langle\varepsilon_5\rangle$ from the MC-KLN model are all significantly larger than those from the MC-Glauber model. In contrast, $\langle\varepsilon_3\rangle$ is numerically very similar for the two models over most of the impact parameter range. The viscous suppression of triangular flow v_3 may thus allow for a determination of the QGP shear viscosity $(\eta/s)_{\mathrm{QGP}}$ that is free from the large model uncertainties that arise from the different MC-Glauber and MC-KLN ellipticities when using v_2 for such an extraction [49].
– The second and fourth order eccentricities ε_2 and ε_4 are strongly correlated by collision geometry, and v_4 receives strong contributions even from a purely elliptical deformation of the final flow velocity distribution. These complications make v_4 a poor candidate for systematic studies of viscous effects on the evolution of collective flow. Similar comments apply to v_5 since it couples via mode-coupling to triangularity from fluctuations and to ellipticity from collision geometry. This mixture of contributions from conceptually different origins complicates a systematic analysis. In general, flow coefficients v_n of high harmonic order ($n > 3$) show poor correlation with the eccentricity coefficients ε_n of the same harmonic order, except for very central collisions where all eccentricities are driven by fluctuations alone (and not by overlap geometry).
– In spite of non-linear mode-coupling effects, the basic response of elliptic flow v_2 to ellipticity ε_2, and of triangular flow v_3 to triangularity ε_3, is approximately linear. These two observables thus remain prime candidates for systematic studies of viscous effects on collective hydrodynamic flow.
– Event-by-event hydrodynamics generates harder p_T-spectra for the emitted hadrons than single-shot hydrodynamic evolution of the corresponding averaged initial profile. This is due to additional radial flow generated by large pressure gradients arising from "hot spots" in the initial fluctuating density distribution. The hardening effect is particularly strong in peripheral collisions which produce small fireballs that fluctuate strongly.
– Event-by-event hydrodynamic evolution of fluctuating initial conditions leads to smaller average elliptic flow than obtained by evolving the corresponding averaged initial condition in a single shot. This suppression depends somewhat on collision centrality, and for ideal fluids it is generically of order 4-5% for pions and 8-10% for protons. The effect is sufficiently large to lead to a significant over-estimate of the fluid's specific shear viscosity if one extracts it from elliptic flow measurements by comparing with single-shot hydrodynamic simulations. Even though we expect the discrepancy between event-by-event and single-shot hydrodynamics to decrease a bit in viscous fluid dynamics, we believe that a quantitatively precise experimental determination of η/s from collective flow data will require comparison with event-by-event hydrodynamical calculations.

Acknowledgments

We gratefully acknowledge fruitful discussions with and valuable comments from Mike Lisa, Matt Luzum, Jean-Yves Ollitrault, Art Poskanzer, Chun Shen, Raymond Snellings, Huichao Song, Sergei Voloshin, and especially Derek Teaney whose question at a recent workshop prompted the study of single-particle spectra presented in Sec. V A. Special thanks go to Matt Luzum and Art Poskanzer for pointing out logical errors in our analysis as presented in the first version of this paper. This work was supported by the U.S. Department of Energy under Grants No. DE-SC0004286 and (within the framework of the JET Collaboration) DE-SC0004104.

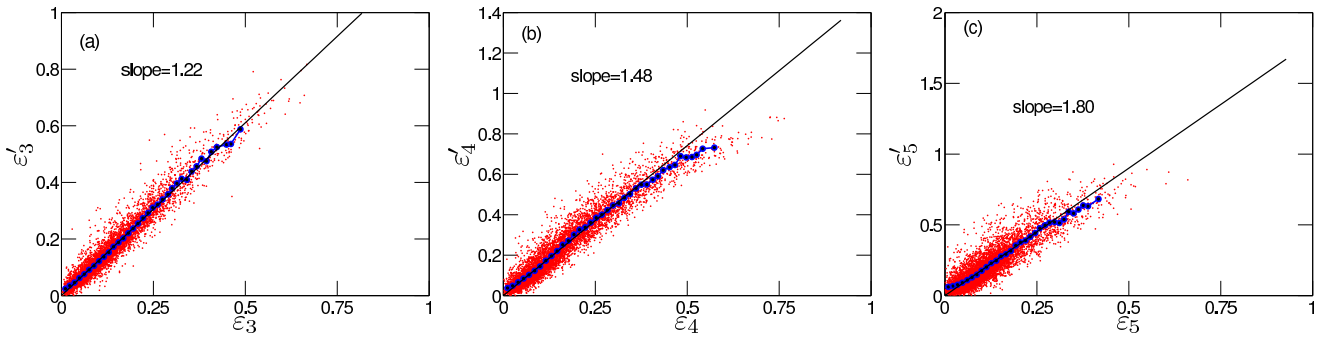


FIG. 16: (Color online) Correlation between ε_n and ε'_n, for $n=2$, 3, 4 (panels (a-c)). The blue dots are bin averages for bins that contain more than 10 events. The thick black lines are linear fits.

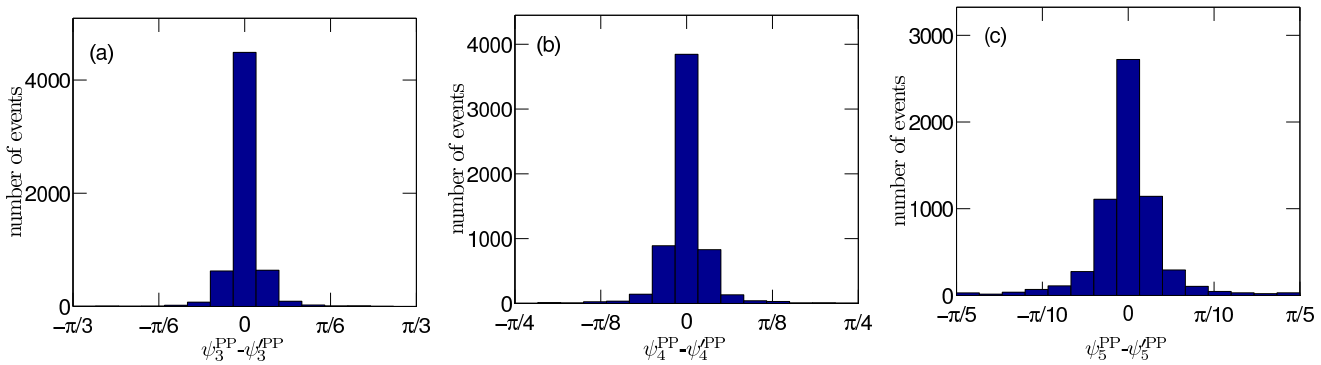


FIG. 17: (Color online) Event-by-event correlation between the participant plane angles associated with r^2- and r^n-weighted eccentricities for harmonic orders $n=3$, 4, and 5 (panels (a)-(c)).

Appendix A: Comparison between eccentricities defined with r^2 and r^n weights

We here present a brief comparison between the r^2-weighted eccentricity coefficients ε_n (Eq. (17)) and the r^n-weighted ε'_n (Eq. (17)), as well as their associated angles $\psi_n^{\rm PP}$ and $\psi_n'^{\rm PP}$. Fig. 16 shows a scatter plot of ε'_n vs. ε_n for $n=3,4,5$. One observes approximate proportionality ($\varepsilon'_3 \approx 1.22\,\varepsilon_3$, $\varepsilon'_4 \approx 1.48\,\varepsilon_4$, $\varepsilon'_5 \approx 1.80\,\varepsilon_5$) over most of the eccentricity range, with slopes that increase with n. So where Fig. 5 shows a decrease of ε_n with increasing n at large impact parameters, the same is not true for the ε'_n [20]. On the other hand, the linear relations between ε'_n vs. ε_n imply that the relations between v_n and ε'_n will look qualitatively the same as those between v_n and ε_n in Fig. 9, with appropriately rescaled horizontal axes.

At the same time the participant plane angles associated with r^2-weighted and r^n-weighted eccentricities are tightly correlated, as shown in Fig. 17. For given n, the angles $\psi_n^{\rm PP}$ and $\psi_n'^{\rm PP}$ fluctuate around each other, with a variance that increases with n, on account of the decreasing values of ε_n. From a practical point of view, we therefore consider both definitions as equivalent, and choosing between them is a matter of personal preference.

[1] U. Heinz and P. F. Kolb, Nucl. Phys. **A702**, 269 (2002).
[2] P. Romatschke and U. Romatschke, Phys. Rev. Lett. **99**, 172301 (2007); M. Luzum and P. Romatschke, Phys. Rev. C **78**, 034915 (2008).
[3] H. Song and U. Heinz, Phys. Rev. C **78**, 024902 (2008).
[4] R. A. Lacey *et al.*, Phys. Rev. C **82**, 034910 (2010).
[5] H. Song, S. A. Bass, U. Heinz, T. Hirano and C. Shen, Phys. Rev. Lett. **106**, 192301 (2011).
[6] H. Song, S. A. Bass, U. Heinz, T. Hirano, C. Shen, Phys. Rev. C **83**, 054910 (2011).
[7] D. Teaney, Phys. Rev. C **68**, 034913 (2003); R. A. Lacey and A. Taranenko, PoS **CFRNC2006**, 021 (2006); R. A. Lacey *et al.*, Phys. Rev. Lett. **98**, 092301 (2007); A. Adare *et al.*, Phys. Rev. Lett. **98**, 172301 (2007); H.-J. Drescher, A. Dumitru, C. Gombeaud, and J.-Y. Ollitrault, Phys. Rev. C **76**, 024905 (2007); K. Dusling and D. Teaney, Phys. Rev. C **77**, 034905 (2008); Z. Xu, C. Greiner, and H. Stöcker, Phys. Rev. Lett. **101**, 082302 (2008); D. Molnar and P. Huovinen, J. Phys. G **35**, 104125 (2008); R. A. Lacey, A. Taranenko and R. Wei, in *Proc. 25th Winter Workshop on Nuclear Dynamics*, W. Bauer, R. Bellwied, and J.W. Harris (eds.), (EP Systema, Budapest, 2009) p. 73 [arXiv:0905.4368]; K. Dusling, G. D. Moore, and D. Teaney, Phys. Rev. C **81**, 034907

(2010); A. K. Chaudhuri, J. Phys. G **37**, 075011 (2010).
[8] H. Song and U. Heinz, Phys. Lett. **B658**, 279 (2008); Phys. Rev. C **77**, 064901 (2008); H. Song, Ph.D. thesis, The Ohio State University, 2009 [arXiv:0908.3656 [nucl-th]].
[9] H. Song and U. Heinz, J. Phys. G **36**, 064033 (2009).
[10] T. Hirano, U. Heinz, D. Kharzeev, R. A. Lacey, and Y. Nara, Phys. Lett. **B636**, 299 (2006).
[11] T. Hirano and Y. Nara, Phys. Rev. C **79**, 064904 (2009); Nucl. Phys. **A830**, 191c (2009).
[12] T. Hirano, P. Huovinen, Y. Nara, Phys. Rev. C **83**, 021902 (2011); and arXiv:1012.3955 [nucl-th].
[13] M. Miller and R. Snellings, arXiv:nucl-ex/0312008; B. Alver *et al.*, Phys. Rev. Lett. **104**, 142301 (2010).
[14] B. Alver *et al.* [PHOBOS Collaboration], Int. J. Mod. Phys. **E16**, 3331 (2007); J. Phys. G **35**, 104101 (2008); and Phys. Rev. C **81**, 034915 (2010).
[15] P. Sorensen [STAR Collaboration], J. Phys. G **35**, 104102 (2008).
[16] J. Y. Ollitrault, A. M. Poskanzer and S. A. Voloshin, Phys. Rev. C **80**, 014904 (2009).
[17] R. S. Bhalerao, J. -Y. Ollitrault, Phys. Lett. **B641**, 260 (2006).
[18] H. -J. Drescher, Y. Nara, Phys. Rev. C **76**, 041903 (2007).
[19] B. Alver and G. Roland, Phys. Rev. C **81**, 054905 (2010).
[20] G.-Y. Qin, H. Petersen, S. A. Bass, and B. Müller, Phys. Rev. C **82**, 064903 (2010).
[21] R. A. Lacey *et al.*, Phys. Rev. C **83**, 044902 (2011).
[22] S. A. Voloshin, A. M. Poskanzer, A. Tang, and G. Wang, Phys. Lett. **B659**, 537 (2008).
[23] B. Alver *et al.*, Phys. Rev. C **77**, 014906 (2008).
[24] S. A. Voloshin, A. M. Poskanzer and R. Snellings, in *Relativistic Heavy Ion Physics*, Landolt-Börnstein New Series, Vol. I/23, edited by R. Stock (Springer Verlag, New York, 2010), Chap. 5 [arXiv:0809.2949 [nucl-ex]].
[25] L. Yi, F. Wang, and A. Tang, arXiv:1101.4646 [nucl-ex].
[26] B. H. Alver, C. Gombeaud, M. Luzum, and J. Y. Ollitrault, Phys. Rev. C **82**, 034913 (2010).
[27] R. Andrade, F. Grassi, Y. Hama, T. Kodama and O. Socolowski, Phys. Rev. Lett. **97**, 202302 (2006); R. P. G. Andrade, Y. Hama, F. Grassi, O. Socolowski and T. Kodama, Braz. J. Phys. **37**, 99 (2007); R. Andrade, F. Grassi, Y. Hama, T. Kodama and O. Socolowski, Braz. J. Phys. **37**, 717 (2007); R. P. G. Andrade, F. Grassi, Y. Hama, T. Kodama, and W. L. Qian, Phys. Rev. Lett. **101**, 112301 (2008).
[28] H. Petersen and M. Bleicher, Phys. Rev. C **81**, 044906 (2010); H. Petersen, G.-Y. Qin, S. A. Bass, and B. Müller, Phys. Rev. C **82**, 041901 (2010).
[29] H. Holopainen, H. Niemi, and K. J. Eskola, Phys. Rev. C **83**, 034901 (2011), and Nucl. Phys. A **855**, 486 (2011).
[30] B. Schenke, S. Jeon, C. Gale, Phys. Rev. Lett. **106**, 042301 (2011).
[31] R. Chatterjee, H. Holopainen, T. Renk, and K. J. Eskola, Phys. Rev. C **83**, 054908 (2011).
[32] P. Sorensen, J. Phys. G **37**, 094011 (2010); A. Mocsy and P. Sorensen, arXiv:1008.3381 [hep-ph]; P. Sorensen, B. Bolliet, A. Mocsy, Y. Pandit and N. Pruthi, arXiv:1102.1403 [nucl-th].
[33] M. L. Miller, K. Reygers, S. J. Sanders and P. Steinberg, Ann. Rev. Nucl. Part. Sci. **57**, 205 (2007).
[34] D. Kharzeev, M. Nardi, Phys. Lett. **B507**, 121 (2001); D. Kharzeev, E. Levin, Phys. Lett. **B523**, 79 (2001).
[35] H. J. Drescher and Y. Nara, Phys. Rev. C **75**, 034905 (2007); *ibid.* **76**, 041903(R) (2007).
[36] P. F. Kolb and U. Heinz, in *Quark-Gluon Plasma 3*, edited by R. C. Hwa and X.-N. Wang (World Scientific, Singapore, 2004), p. 634 [arXiv:nucl-th/0305084];
[37] S. Voloshin and Y. Zhang, Z. Phys. **C70**, 665 (1996).
[38] D. Teaney and L. Yan, arXiv:1010.1876 [nucl-th].
[39] F. Cooper and G. Frye, Phys. Rev. D **10**, 186 (1974).
[40] P. Huovinen, P. Petreczky, Nucl. Phys. **A837**, 26 (2010).
[41] C. Shen, U. Heinz, P. Huovinen and H. Song, Phys. Rev. C **82**, 054904 (2010).
[42] M. Luzum, Phys. Rev. C **83**, 044911 (2011).
[43] H. Song, S. A. Bass and U. Heinz, Phys. Rev. C **83**, 054912 (2011).
[44] C. Shen, U. Heinz, P. Huovinen and H. Song, arXiv:1105.3226 [nucl-th].
[45] Y. Bai, Ph.D. Thesis, Nikhef and Utrecht University, The Netherlands (2007); B. I. Abelev *et al.* [STAR Collaboration], Phys. Rev. C **77**, 054901 (2008).
[46] K. Aamodt *et al.* [ALICE Collaboration], Phys. Rev. Lett. **105**, 252302 (2011).
[47] K. Aamodt *et al.* [ALICE Collaboration], arXiv:1105.3865 [nucl-ex]; and R. Snellings, talk presented at the "Quark Matter 2011" Conference, Annecy, France, May 23-28, 2011.
[48] C. Shen, B. Schenke, and U. Heinz, in preparation.
[49] U. Heinz and Zhi Qiu, in preparation.
[50] P. F. Kolb and U. Heinz, unpublished notes (Oct. 2003); N. Borghini and J.-Y. Ollitrault, Phys. Lett. **B642**, 227 (2006).
[51] M. Luzum, C. Gombeaud, and J.-Y. Ollitrault, Phys. Rev. C **81**, 054910 (2010).